Article

Current Biology

KIF13B controls ciliary protein content by promoting endocytic retrieval and suppressing release of large extracellular vesicles from cilia

Graphical abstract

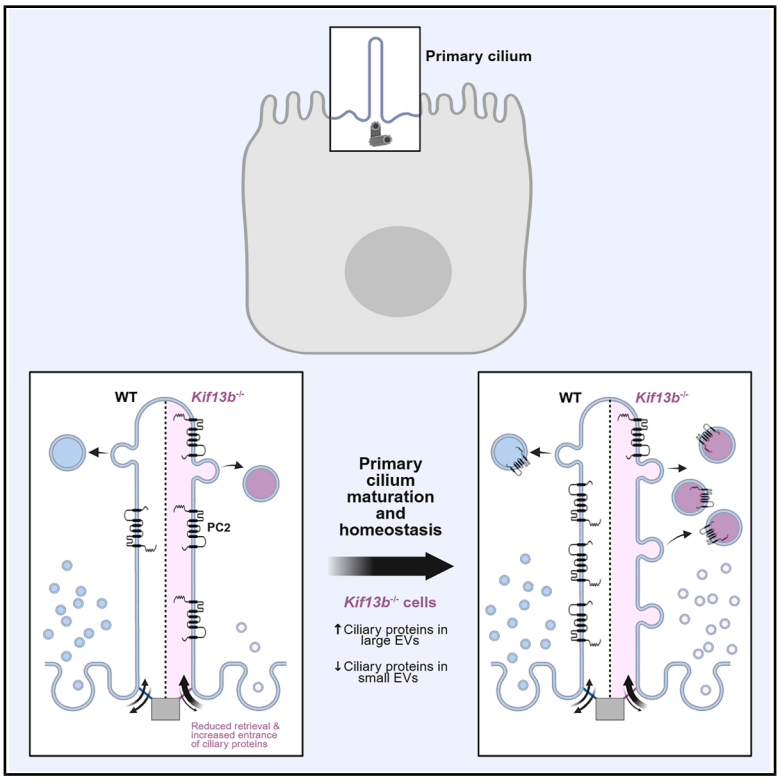

Authors

Csenge K. Rezi, Alina Frei, Fabiola Campestre, ..., Zeinab Anvarian, Helen L. May-Simera, Lotte B. Pedersen

Correspondence

may-simera@uni-mainz.de (H.L.M.-S.), lbpedersen@bio.ku.dk (L.B.P.)

In brief

Rezi et al. show that kinesin-3 KIF13B regulates ciliary protein content by promoting endocytic retrieval and small extracellular vesicle (EV) release of ciliary proteins while suppressing their release in large EVs. Furthermore, they identify PC2, CCDC92, CCDC198, HGS, and ZDHHC5 as ciliary proteins and EV cargoes regulated by KIF13B.

Highlights

- KIF13B downregulates ciliary protein content in kidney epithelial cells
- Ciliary PC2, CCDC92, HGS, and ZDHHC5 homeostasis is regulated by KIF13B
- Accumulated proteins of Kif13b$^{-/-}$ cilia are shed in large extracellular vesicles
- Ciliary proteins are depleted from small extracellular vesicles of Kif13b$^{-/-}$ cells

Rezi et al., 2025, Current Biology *35*, 4651–4667
October 6, 2025
https://doi.org/10.1016/j.cub.2025.08.022

CellPress

Current Biology

CellPress
OPEN ACCESS

Article

KIF13B controls ciliary protein content by promoting endocytic retrieval and suppressing release of large extracellular vesicles from cilia

Csenge K. Rezi,[1,4,8] Alina Frei,[2,8] Fabiola Campestre,[1,8] Karsten Boldt,[3] Benjamin Mary,[1] Anna Maria Fixdahl,[1] Anna-Louise With Petersen,[1] Aurelien Sicot,[1,5] Christina R. Berggreen,[1] Julie Laplace,[1,6] Søren L. Johansen,[1] Julie K.T. Sørensen,[1,7] Mohamed Chamlali,[1] Martin W. Berchtold,[1] Søren T. Christensen,[1] Zeinab Anvarian,[1] Helen L. May-Simera,[2,*] and Lotte B. Pedersen[1,9,*]

[1]Department of Biology, University of Copenhagen, Universitetsparken 13, 2100 Copenhagen Ø, Denmark
[2]Institute of Molecular Physiology, Johannes Gutenberg-University, 55122 Mainz, Germany
[3]Core Facility for Medical Proteomics and Institute for Ophthalmic Research, Center for Ophthalmology, University of Tübingen, 72076 Tübingen, Germany
[4]Present address: Department of Microbiology & Immunology, Baxter Labs, Stanford University, Center for Clinical Sciences Research, Rm. 3205b, 269 Campus Drive, Stanford, CA 94305-5175, USA
[5]Present address: Sim&Cure, 95 rue Pierre Flourens, Bâtiment H, 34000 Montpellier, France
[6]Present address: École Normale Supérieure Paris-Saclay, Department of Biology, 4 Avenue des Sciences, 91190 Gif-sur-Yvette, France
[7]Present address: AJ Vaccines A/S, Artillerivej 5, 2300 Copenhagen S, Denmark
[8]These authors contributed equally
[9]Lead contact
*Correspondence: may-simera@uni-mainz.de (H.L.M.-S.), lbpedersen@bio.ku.dk (L.B.P.)
https://doi.org/10.1016/j.cub.2025.08.022

SUMMARY

Dynamic control of ciliary membrane protein content is crucial for the organelle's homeostasis and signaling function and involves removal of ciliary components by intraflagellar transport (IFT) and BBSome-mediated export, endocytic retrieval, and/or extracellular vesicle (EV) shedding. We report that the kinesin-3 motor KIF13B regulates ciliary protein composition and EV shedding in cultured kidney epithelial cells, with effects that vary over time. In early stages of ciliation, Kif13b$^{-/-}$ cells aberrantly accumulate polycystin-2 (PC2) within cilia and release large EVs enriched with CCDC198 and the centriole distal appendage protein CCDC92, which also localizes to the ciliary tip. These cells also produce fewer small EVs through the neutral sphingomyelinase 2 pathway. Upon cilia maturation, Kif13b$^{-/-}$ cells accelerate large EV release of numerous ciliary proteins, including PC2, BBSome, and IFT components, which correlates with gradual depletion of CCDC92 and PC2 from the ciliary tip and shaft, respectively. Furthermore, over time, Kif13b$^{-/-}$ cells show an upregulation in the release of small EVs, which differ in composition from wild-type small EVs. Specifically, mutant small EVs lack several proteins that are enriched in small EVs from BBSome-deficient cells, including palmitoyl transferase ZDHHC5, which localizes to cilia where it accumulates upon BBSome dysfunction and regulates ciliary length and PC2 levels. Our results suggest that KIF13B acts at the level of centriole distal appendages to limit ciliary protein entry and promote endocytic retrieval downstream of the BBSome, thereby suppressing EV release from cilia. Furthermore, the ciliary localization of CCDC198 and ZDHHC5 indicates they are potential novel ciliopathy candidates.

INTRODUCTION

Primary cilia are antenna-like sensory organelles that protrude from the cell surface and play important roles in coordinating developmental and homeostatic signaling pathways that regulate cell behavior, division, and differentiation.[1,2] Ciliary defects cause ciliopathies, including several diseases with renal phenotypes, e.g., Bardet-Biedl Syndrome (BBS) and polycystic kidney disease (PKD).[2,3] The ciliary membrane houses specific proteins and lipids that function in signaling.[4,5] For example, in kidney epithelial cells, the transmembrane proteins polycystin-1 (PC1) and polycystin-2 (PC2), encoded by the autosomal dominant (AD) PKD genes *PKD1* and *PKD2*, respectively,[6,7] localize to primary cilia.[8,9] Here they form a calcium-permeable cation channel complex required for normal renal tubular structure and function. Variants in *PKD1*, *PKD2*, or other genes that impair ciliary polycystin localization may cause ADPKD, indicating that appropriate ciliary targeting and homeostasis of polycystins are critical for kidney development, homeostasis, and function.[10–12] After its synthesis, PC2 is thought to be transported via recycling endosomes or the plasma membrane to the ciliary base, where it crosses the transition zone and enters the cilium.[11,13,14] Subsequently, ciliary PC2 levels are downregulated by retrieval, endocytic sorting, and release of

PC2-containing extracellular vesicles (EVs) to ensure organelle homeostasis.[11]

EVs are released by many cell types and mediate intercellular transport of macromolecules to regulate physiological and pathological processes. Two major subtypes of EVs have been categorized based on their origin: exosomes, which are small (50–150 nm in diameter) and derived from the multivesicular body (MVB), and ectosomes or microvesicles, which can be up to several micrometers in diameter and bud directly from the plasma membrane.[15,16] Both primary and motile cilia shed EVs to regulate ciliary membrane homeostasis and/or intercellular signaling.[17–20] It is thought that cilia-derived EVs are ectosomes, generated by outward budding of the ciliary membrane,[17] which can range in size and content depending on their ciliary release site.[21] Hereafter, we designate exosomes and small ectosomes as small EVs and larger ectosomes as large EVs.

The cellular origin of specific EV subtypes is difficult to distinguish in biochemical preparations, and similar EV cargo sorting and biogenesis pathways may be employed dynamically to generate diverse subpopulations of small and large EVs in a context-dependent manner.[15,16] Such pathways include (1) the ESCRT pathway involving HGS- and STAM-mediated sorting of ubiquitylated cargoes, (2) the ALIX-syntenin pathway, (3) the GW4869-sensitive pathway involving neutral sphingomyelinase 2 (nSMase2)/ceramide-dependent EV formation of cargoes concentrated in lipid rafts enriched for flotillins and cholesterol, and (4) actin-mediated formation of membrane blebs to generate large EVs.[16]

While the mechanisms involved in ciliary EV cargo sorting and biogenesis are not well understood,[18,20] it is known that the actin cytoskeleton promotes EV release from cilia,[22–26] whereas the BBSome, a complex of BBS proteins that functions as a cargo adaptor for ubiquitinated membrane proteins during retrograde intraflagellar transport (IFT),[27–29] suppresses the process, both during homeostatic and signal-dependent EV release.[4,22,26,30,31] For example, combined depletion of BBS4 and BBS5 from human retinal pigment epithelial (RPE1) cells or *Caenorhabditis elegans* sensory neurons caused aberrant ciliary accumulation of the EV cargo PC2 due to impaired retrieval of ubiquitinated PC2 from cilia.[32] Moreover, studies in *C. elegans* male sensory neurons indicated that downregulation of ciliary polycystins involves the ESCRT-0 proteins HGS and STAM, which function on early endosomes to direct the PC1-PC2 complex for lysosomal degradation.[33] This pathway may also involve RAB5 and caveolin-1 (CAV1), which, together with Rabenosyn-5 and VPS45, promote endocytic sorting of PC2 at the periciliary membrane compartment.[32,34] In addition, *C. elegans* sensory neuronal cilia exhibit environmental release of polycystin-containing EVs via a mechanism involving the kinesin-3 motor protein KLP-6. In *klp-6* mutant animals, such EVs are not released into the environment, causing excessive shedding of EVs into the glial lumen surrounding the ciliary base.[35] The release of polycystin-containing EVs from cilia is evolutionarily conserved, as polycystin homologs were detected in cilia-derived EVs from *Chlamydomonas*[36,37] and in EVs from human urine[38] and the mouse embryonic node.[39] However, the mechanisms underlying ciliary polycystin homeostasis and EV release in vertebrates remain incompletely understood.

We previously showed that a mammalian homolog of KLP-6, the kinesin-3 motor protein KIF13B, localizes to primary cilia of RPE1 cells, where it mediates formation of a CAV1-enriched membrane domain at the ciliary base, thereby regulating Sonic hedgehog signaling.[40] KIF13B also moves transiently within and is occasionally released from such cilia in EV-like particles.[41]

Here, we demonstrate that KIF13B regulates ciliary protein composition and EV release in mouse cortical collecting duct (mCCD) cells in a time-dependent manner. In early stages of ciliation, Kif13b$^{-/-}$ cells aberrantly accumulate PC2, FLOT1, and HGS within cilia, produce fewer small EVs, and release large EVs enriched for CCDC198 (also known as FAME) and for the centriole distal appendage protein (DAP) CCDC92, which also localizes to the ciliary tip. Upon cilia maturation, the large EV content of numerous ciliary proteins such as PC2, BBSome, and IFT components is upregulated in the Kif13b$^{-/-}$ cells, which correlates with ciliary depletion of PC2 and loss of CCDC92 from the ciliary tip. Kif13b$^{-/-}$ cells also upregulate the rate of small EV release over time, but these EVs differ in composition from wild-type (WT)-derived small EVs by lacking several proteins that are conversely enriched in small EVs from BBSome-deficient cells. These include the palmitoyl transferase ZDHHC5, which localizes to cilia, accumulates in cilia upon BBSome inactivation, and controls ciliary length and PC2 levels.

RESULTS

KIF13B loss alters ciliary PC2 levels

To test if KIF13B regulates ciliary PC2 homeostasis and EV shedding, we knocked it out in mCCD cells (Figure 1A; Figure S1A). Consistent with previous work[42,43] mCCD cells formed primary cilia upon serum starvation for 24 or 72 h, and loss of KIF13B had little effect on ciliary frequency or length under these conditions (Figures S1B–S1D). Total cellular levels of PC2 in Kif13b$^{-/-}$ cells were also unaffected, both for cells grown in the presence of serum (+ fetal bovine serum [FBS]) or depleted of serum for 24, 48, or 72 h (Figures 1A and 1B; Figure S1E). Next, we analyzed the ciliary localization of PC2 in WT and Kif13b$^{-/-}$ cells by immunofluorescence microscopy analysis (IFM). Using a previously described anti-PC2 antibody[44] to stain for PC2 in 24 h serum-starved cells, we observed significant accumulation of PC2 within cilia of Kif13b$^{-/-}$ cells compared with WT (Figures 1C and 1D). Stable expression of mCherry-KIF13B in Kif13b$^{-/-}$ cells (Figures S1F and S1G) rescued this phenotype (Figures 1C and 1D), and similar results were obtained using another PC2 antibody (Figures 1E and 1F). By contrast, IFM of 72 h serum-starved cells revealed significantly lower ciliary PC2 levels in Kif13b$^{-/-}$ cells compared with WT and rescue lines (Figures 1E and 1F). Thus, KIF13B regulates ciliary PC2 levels in a time-dependent manner.

Ciliary proteins accumulate in large EVs from Kif13b$^{-/-}$ cells

To explore whether KIF13B affects EV shedding of PC2 or other ciliary proteins, we purified large EVs from 24- or 72-h serum-starved WT and Kif13b$^{-/-}$ cells by centrifugation (Figure 2A), validated these EV samples by transmission electron microscopy (TEM) and nanoparticle tracking analysis (NTA) (Figures S2A and S2B), and assessed their protein content by

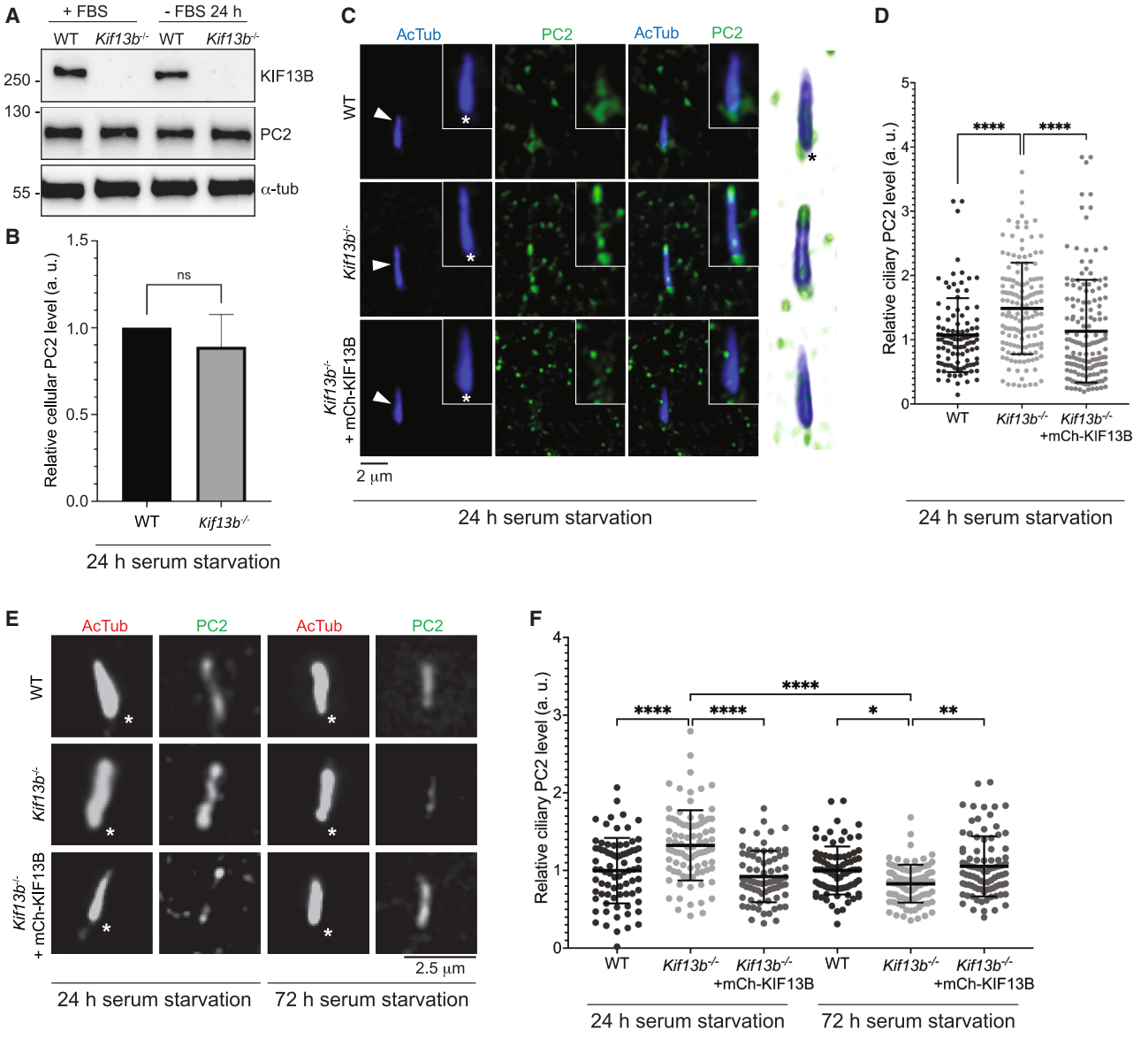

Figure 1. Ciliary PC2 localization in mCCD cells

(A) Western blots of WT and Kif13b$^{-/-}$ mCCD cells grown with (+) or without (–) FBS for 24 h. α-Tubulin (α-tub): loading control. Molecular mass markers are in kDa.

(B) Quantification of relative cellular PC2 levels in WT and Kif13b$^{-/-}$ cells, based on western blots. Graphs show mean ± SD (n = 3), and significance was determined using an unpaired, two-tailed Student's t test.

(C and E) IFM of mCCD cells, using two different PC2 antibodies. Acetylated α-tubulin (AcTub) marks the cilium (arrowheads), and asterisks mark the ciliary base. Insets in (C) show enlargement of the cilium-centrosome axis, and the rightmost panels are 3D renderings thereof. mCh-KIF13B: mCherry-KIF13B.

(D and F) Quantification of relative ciliary PC2 staining intensities, based on images as in (C) and (E), respectively. Mean fluorescence intensity (MFI) of PC2 was measured for 50 cilia per cell line per experiment and normalized to that of the WT 24 h mean value. a.u., arbitrary units. Graphs show mean ± SD (n = 3), and significance was determined using the nonparametric Kruskal-Wallis test, followed by Dunn's multiple pairwise-comparison test.

See also Figure S1.

mass spectrometry (MS). Proteins that were significantly altered in abundance between WT and Kif13b$^{-/-}$ samples were divided into two tiers based on stringency criteria (see STAR Methods). After 24 h, we identified seven tier 1 proteins that were significantly altered in abundance in large EVs, four of which (CTPS2, POFUT2, DCTN6, and NHLC2) were depleted, the remaining three (CCDC198, CCDC92, and MLF2) being enriched in mutant-derived EV samples compared with controls (Figure 2B; Data S1A). For the 72 h large EV samples, we identified 72 tier 1 proteins that were significantly altered, including enrichment of numerous ciliary proteins like IFT and BBSome components in mutant EVs (Figure 2C; Data S1B). Gene Ontology (GO) analysis of the tier 1 and tier 2 proteins in the latter, focusing on the cellular component category, identified

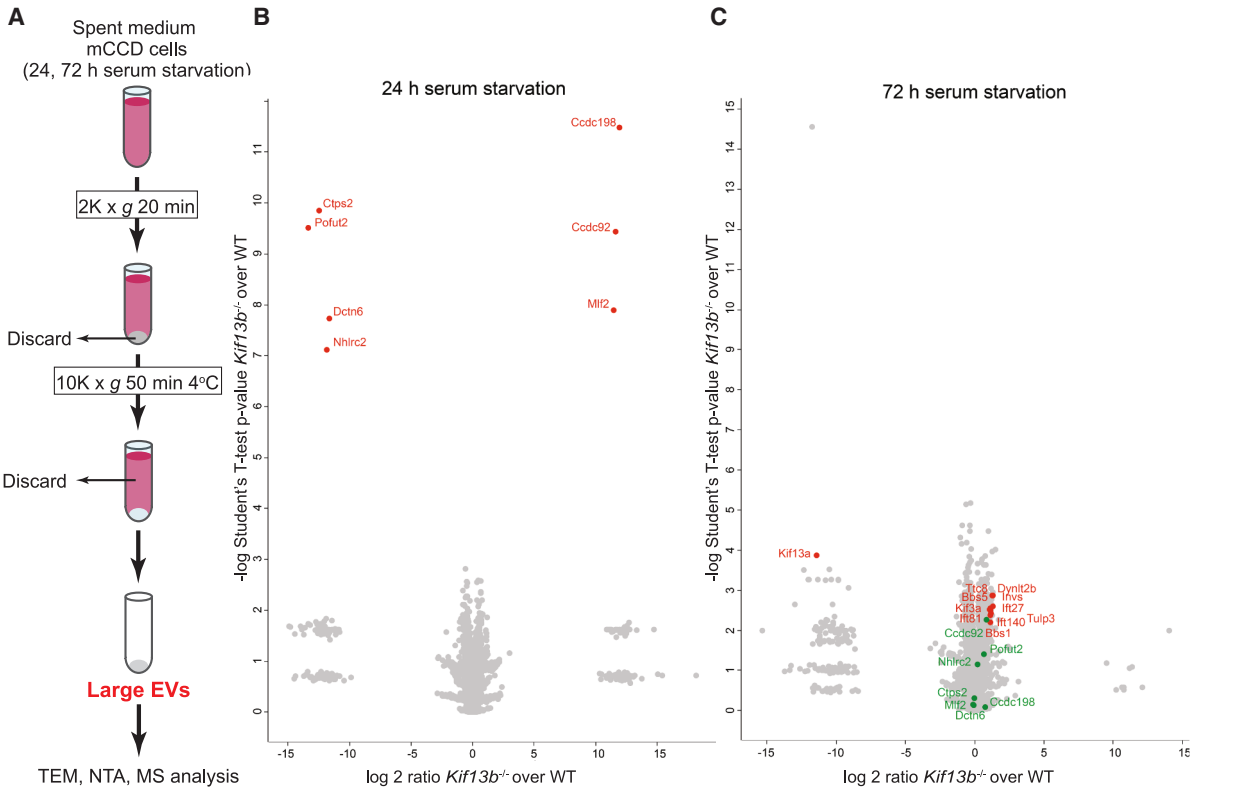

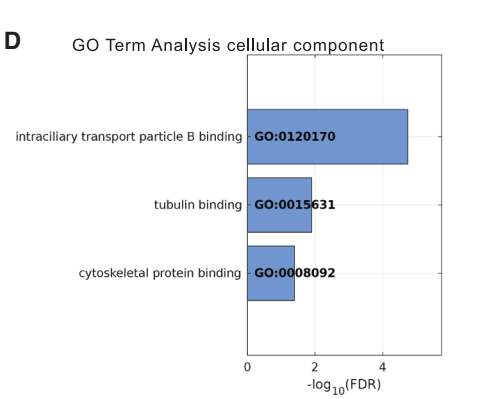

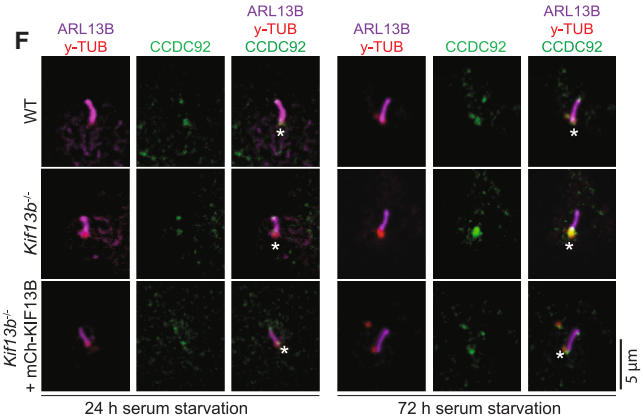

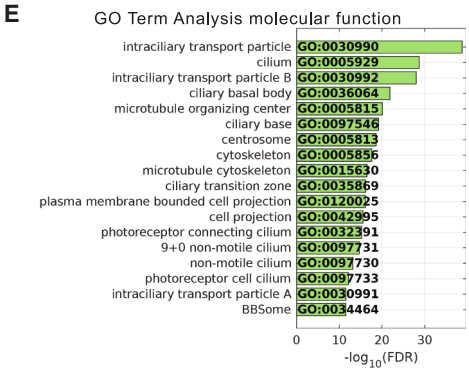

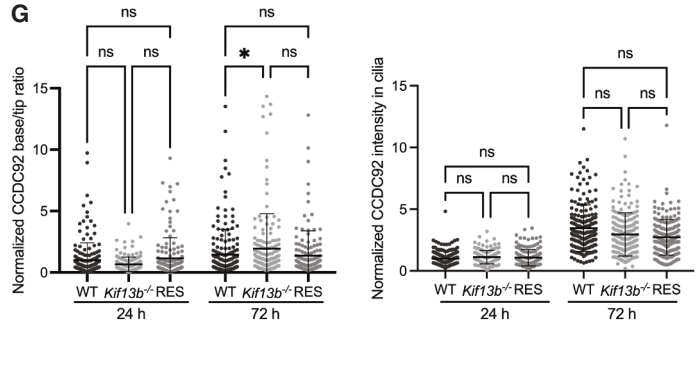

(legend on next page)

"intraciliary transport particle B binding" as the most highly enriched GO term in this dataset, followed by "tubulin binding" and "cytoskeletal binding" (Figure 2D; Data S3A). Similarly, GO analysis for the molecular function category identified "intraciliary transport particle" and "cilium" as the most highly enriched GO terms among this dataset (Figure 2E; Data S3A). PC2 and PC1 were also significantly enriched in the 72 h large EV samples from Kif13b$^{-/-}$ cells compared with WT (tier 2 hits; Data S1B) but were unchanged in relative abundance in the 24 h large EV samples. We did not detect KIF13B in large EVs under these conditions (but see Figure S3 and below).

To test if altered protein content of large EVs from Kif13b$^{-/-}$ cells could stem from increased ciliary fragmentation, we analyzed ciliary morphology in 24 or 72 h serum-deprived WT, Kif13b$^{-/-}$, and rescue lines by scanning electron microscopy (SEM). Average ciliary length was around 2 μm for all conditions, with a tendency for longer cilia in 72 h serum-starved Kif13b$^{-/-}$ cells (Figures S1D, S2C, and S2D). Membrane bulges at the tip or side of cilia were observed for all conditions, with significantly more side bulges seen in 72 h serum-starved Kif13b$^{-/-}$ cilia compared with WT. A similar trend was observed at the 24 h time point, although the difference was not statistically different (Figures S2C–S2F). These membrane bulges resemble budding EVs previously observed in cilia of murine inner medullary collecting duct (IMCD)3, primary biliary epithelial and neuroepithelial cells, as well as Madin-Darby canine kidney (MDCK) and RPE1 cells,[22,38,45–49] although we cannot exclude that they represent vesicles docking to, and not budding from, cilia. In sum, loss of KIF13B in mCCD cells has limited impact on ciliary length and morphology but causes enrichment of PC2 and other ciliary proteins in large EVs over time and increased membrane bulging from the side of cilia.

Ciliary localization of KIF13B, CCDC92, and CCDC198

We tested whether KIF13B localizes to cilia of mCCD cells by live imaging of Kif13b$^{-/-}$ cells stably expressing mNeonGreen (mNG)-KIF13B (Figures S1F and S1G). In cells serum-starved for 24–48 h, mNG-KIF13B transiently accumulated and moved bidirectionally within 21% of cilia analyzed (n = 72; Video S1), as in RPE1 cells.[41] Similarly, after 72 h of starvation, mNG-KIF13B transiently accumulated and moved within 32% of cilia analyzed (n = 57), occasionally being released from the tip (Video S2). Although the latter observation could be a side effect of mNG-KIF13B overexpression (Figures S1G and S1F), western blotting of EVs purified from spent medium of 72 h serum-starved mCCD cell cultures by centrifugation (large EVs) and lectin-mediated precipitation (small EVs),[50] respectively (Figure S3A), identified KIF13B predominantly in large EVs, whereas ciliary proteins like ARL13B, acetylated α-tubulin, and PC2 were detected in both large and small EV samples under these conditions (Figures S3B and S3C). Thus, KIF13B localizes to cilia of and is present in large EVs from mCCD cells.

Next, we focused on CCDC92 and CCDC198, which were significantly enriched in large EVs from 24 h serum-starved Kif13b$^{-/-}$ cells compared with WT samples (Figure 2B; Data S1A). CCDC92 is a centrosomal DAP that interacts with CEP164 and TTBK2,[51–54] which in turn binds CSNK2A1 that regulates ciliary protein trafficking and EV release in fibroblasts.[54] CCDC198 was linked to mammalian energy balance and kidney physiology,[55] but a ciliary role is unknown. Via IFM, we found that CCDC92 localizes to the base and tip of cilia in mCCD cells (Figure 2F). Total ciliary levels of CCDC92 were unchanged in the Kif13b$^{-/-}$ cells relative to controls, both after 24 and 72 h of serum starvation, but the ciliary base-to-tip ratio of CCDC92 was initially decreased in mutant cells, a phenotype that was reversed at the 72 h time point (Figures 2F and 2G). Live imaging of 24 h serum-starved WT cells transiently expressing GFP-CCDC92 confirmed its ciliary base and tip localization and revealed dynamic movement within cilia (Video S3), with occasional release from the tip (Video S4). In live Kif13b$^{-/-}$ cells, GFP-CCDC92 appeared more static and accumulated at the ciliary tip (Video S5), in line with our IFM results (Figures 2F and 2G). Technical challenges, including cilia drifting out of focus and scarcity of ciliated cells expressing GFP-CCDC92, prevented robust quantification of these results. Nevertheless, combined with our MS data (Figure 2B; Data S1A), these results indicate that KIF13B promotes retention of CCDC92 at the ciliary base, whereas KIF13B loss causes CCDC92 to first accumulate and then be released from the ciliary tip. Consistently, IFM of Kif13b$^{-/-}$ cells revealed CCDC92 in EV-like particles positive for the ciliary marker acetylated α-tubulin (Figure S4C). Similar IFM of CCDC198 showed that it localizes to the plasma membrane, as expected,[55] but also to cilia (Figure S4A). However, we did not detect significant changes in the overall ciliary levels of CCDC198 between Kif13b$^{-/-}$ and WT cells under these conditions (Figure S4B). Thus, KIF13B regulates the ciliary base-to-tip ratio of CCDC192 in a time-dependent manner, and CCDC198 localizes to primary cilia.

KIF13B promotes GW4869-sensitive/ceramide-dependent small EV release

We next investigated the effect of KIF13B loss on small EV release. Small EVs were purified from spent medium of WT

Figure 2. Composition of large EVs

(A) Large EV purification scheme.

(B and C) Volcano plots comparing the protein content of large EVs isolated from WT and Kif13b$^{-/-}$ cells after 24 h (B) and 72 h (C) of serum starvation, based on MS analysis (n = 5). Selected proteins that differ significantly in abundance between mutant and WT samples are in red, and proteins that are significantly altered at 24 h but not at 72 h are in green.

(D and E) GO Term analysis for the categories cellular component (D) and molecular function (E) for proteins significantly altered in abundance in large EVs of Kif13b$^{-/-}$ mCCD cell cultures after 72 h of serum starvation. The tables show the GO terms that are significantly enriched (Fisher's exact test value ≤ 0.05), listed according to their enrichment ratio.

(F) IFM of CCDC92 in mCCD cells, co-stained for ARL13B and γ-tubulin (γ-tub) to label the ciliary membrane and centrioles (asterisk), respectively.

(G) The left graph shows quantification of ciliary base-to-tip ratio (left) or total ciliary staining intensity (right) of CCDC92, based on images as in (F). The right graph shows the MFI of CCDC92 measured for 40–60 cilia per cell line per experiment, normalized to the WT 24 h mean value. Graphs show mean ± SD (n = 3), and significance was determined using the nonparametric Kruskal-Wallis test, followed by Dunn's multiple pairwise-comparison test.

See also Figures S1–S4 and S6, Data S1A, S1B, and S3A, and Videos S1, S2, S3, S4, and S5.

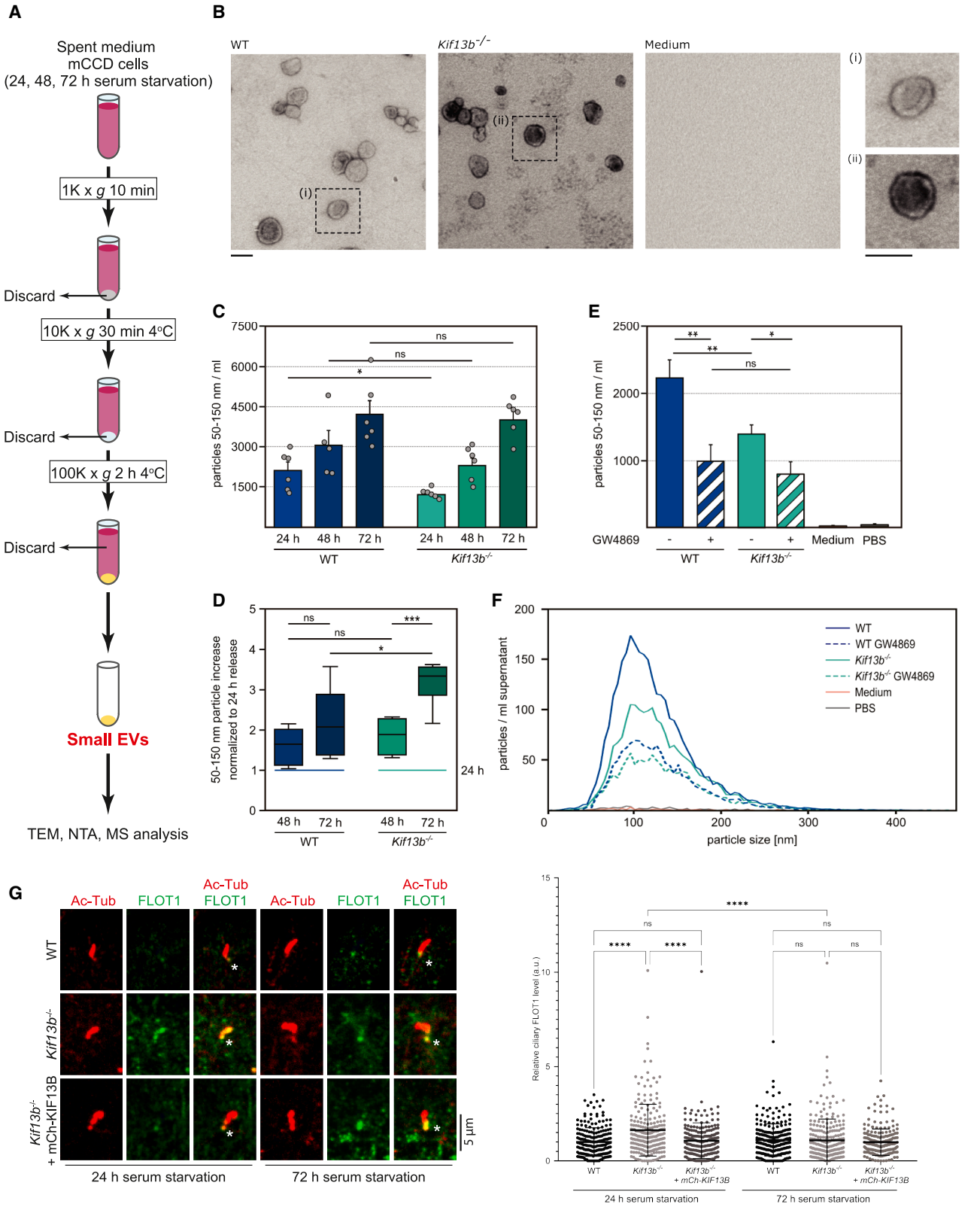

Figure 3. Characterization of small EV release

(A) Small EV purification scheme.

(B) Negative staining and TEM analysis of small EVs from 48 h serum-starved cultures (scale bars, 100 nm).

(legend continued on next page)

and Kif13b$^{-/-}$ cultures following 24, 48, or 72 h of serum starvation (Figure 3A), as validated by TEM (Figure 3B), western blotting for small EV markers (Figure S3D), and NTA, which showed a significant decrease in the number of small EVs released from Kif13b$^{-/-}$ cultures after 24 h, but not 72 h, compared with WT (Figures 3C and 3D). Treatment of 24 h cultures with GW4869, which inhibits nSMase2/ceramide-dependent EV biogenesis,[16] led to an overall reduction in small EV numbers for both cell lines, as expected (Figures 3E and 3F). However, the inhibitory effect of GW4869 treatment on the number of small EVs released from WT cultures was significantly higher compared with that of Kif13b$^{-/-}$ cultures (Figures 3E and 3F), indicating that Kif13b$^{-/-}$ cells are already impaired in small EV biogenesis via this pathway.

N-SMase2/ceramide-dependent EV biogenesis involves localization of cargoes to lipid rafts enriched in flotillins and cholesterol.[16] The ciliary membrane is highly enriched in ceramides,[56,57] KIF13B binds directly to the hydrophobic ceramide backbone of glycosphingolipids,[58] and flotillins localize to the ciliary base of odontoblasts and kidney epithelial cells, where they interact with OFD1, PC1, and PC2.[59] Via IFM we found that FLOT1 localizes to the ciliary base of WT mCCD cells and accumulates within cilia of 24 h, but not 72 h, serum-starved Kif13b$^{-/-}$ cells, and stable expression of mCherry-KIF13B rescued this phenotype (Figures 3G and 3H). The total cellular level of FLOT1 was not affected by KIF13B loss (Figure S3E). Hence, KIF13B regulates ciliary FLOT1 levels in a time-dependent manner, similar to PC2.

KIF13B regulates small EV protein content

To determine if loss of KIF13B affects the protein content of small EVs, we analyzed small EV samples from 24- and 72-h serum-starved WT and Kif13b$^{-/-}$ cultures by MS. For the 24 h small EV samples, three proteins, THBS1, vimentin, and HGS, were significantly depleted from the Kif13b$^{-/-}$ samples compared with WT (Figure 4A; Data S2A). For the 72 h samples, 52 proteins were significantly altered in the Kif13b$^{-/-}$ sample compared with WT, with the majority being depleted from the mutant-derived EVs (Figures 4B and 4D; Data S2B). GO analysis of the latter proteins, focusing on the cellular component category, identified "cytoplasm" and "intracellular anatomical structure" as the most highly enriched GO terms in this dataset (Figure 4C; Data S3B). GO analysis focusing on molecular function "only" identified protein binding (Data S3B). Specific proteins depleted from the 72 h mutant EV samples included TTC8, a BBSome component[27,60]; the acid ceramidase ASAH2; the deubiquitinase STAMBP, which regulates cell surface receptor trafficking at ESCRT-0 positive endosomes by directly binding to the HGS-STAM complex and regulating its ubiquitination status[61]; the ubiquitin E3 ligase ITCH that binds and ubiquitylates several proteins, including HGS and STAM[62]; and the palmitoyltransferase ZDHHC5 (Figure 4B; Data S2B). PC1 and PC2 were also detected in our small EV proteomes of 72 h serum-starved WT and Kif13b$^{-/-}$ cultures but were unchanged in relative abundance in the mutant small EVs compared with WT under these conditions. We did not detect PC1 nor PC2 in small EVs from 24 h serum-starved cultures (Data S2A). Notably, several of the differentially regulated small EV proteins detected in our MS analysis, including THBS1, HGS, and ZDHHC5, were identified in the ciliary proteome of IMCD3 cells.[63] Moreover, HGS and 11 of the proteins that were depleted from the 72 h Kif13b$^{-/-}$ small EV samples were enriched in small EVs purified from *Bbs4* and/or *Bbs6* mutant kidney medullary (KM) cell lines (Figure 4D).[19] We therefore surmised that KIF13B may function downstream of the BBSome to promote endocytic retrieval of HGS and other small EV cargoes from cilia, ultimately leading to their small EV release via MVBs. To test this, we initially focused on HGS, given its known role in regulating ciliary PC2 homeostasis[33] and because HGS interacted directly with FLOT1 in an *in vitro* pull-down assay.[64] Via IFM, we confirmed that HGS localizes to cilia in mCCD cells, primarily at the ciliary base (Figure 4E). Moreover, HGS accumulated significantly within cilia of Kif13b$^{-/-}$ cells compared with WT and rescue lines, both after 24 and 72 h of starvation (Figure 4F), and total cellular levels of HGS were not altered in the mutant (Figure S3E). Thus, KIF13B regulates small EV composition and ciliary HGS levels in a time-dependent manner.

Ciliary localization and function of ZDHHC5

Flotillins are the main palmitoylation substrates of ZDHHC5 in mouse neuronal stem cells.[65] Since ZDHHC5 was depleted and enriched, respectively, in small EVs from 72 h serum-starved Kif13b$^{-/-}$ mCCD cells (Figure 4B; Data S2B) and BBSome-deficient KM cells,[19] we tested if ZDHHC5 localizes to cilia in these cells. IFM of serum-starved WT KM cells showed that ZDHHC5 localizes to the ciliary base, but in the *Bbs4* or *Bbs6* knockout cells, it accumulated significantly along the cilium (Figures 5A and 5B). Furthermore, IFM showed localization of ZDHHC5 to the basal body and cilium of both WT and Kif13b$^{-/-}$ cells and indicated that its ciliary levels are higher at 72 h compared with 24 h of serum starvation (Figures S5A and S5B). There was a trend toward reduced ciliary levels of ZDHHC5 in the 72 h serum-starved Kif13b$^{-/-}$ cells compared with the WT and rescue line, but this change was not statistically significant

(C) NTA profiling of small EVs. Data are represented as mean values, and error bars show SEM (n = 5–6).
(D) Relative increase in small EV release of WT and Kif13b$^{-/-}$ cultures at time points 48 and 72 h, respectively, compared with the 24 h time point. Based on data in (C).
(E and F) NTA profiling of small EVs of mCCD cell cultures incubated with (+) or without (–) GW4869 for 24 h prior to collection of the spent medium (n = 14 for untreated; n = 7 for GW4869; n = 3 for medium; n = 10 for PBS). Data show mean values of particles 50–150 nm in size. Error bars in (E) show SEM. For (C)–(E), statistics were done using the Shapiro-Wilk test and unpaired, two-tailed Student's t test.
(G) IFM of mCCD cells, stained for acetylated α-tubulin (AcTub) and FLOT1. Asterisk marks the ciliary base. mCh-KIF13B: mCherry-KIF13B.
(H) Quantification of relative ciliary FLOT1 levels, based on images as in (G). 40–60 cilia were analyzed per cell line per experiment and normalized to that of WT 24 h mean value. Graphs show mean ± SD (n = 3), and significance was determined using the nonparametric Kruskal-Wallis test, followed by Dunn's multiple pairwise-comparison test.
See also Figures S3 and S6.

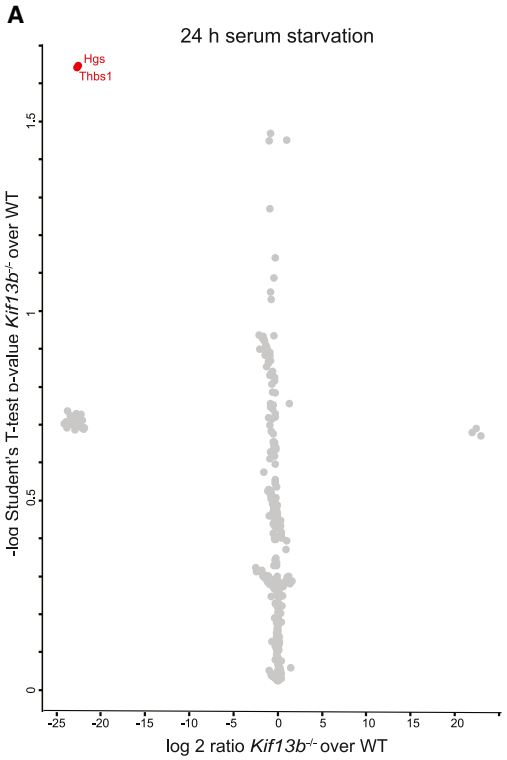

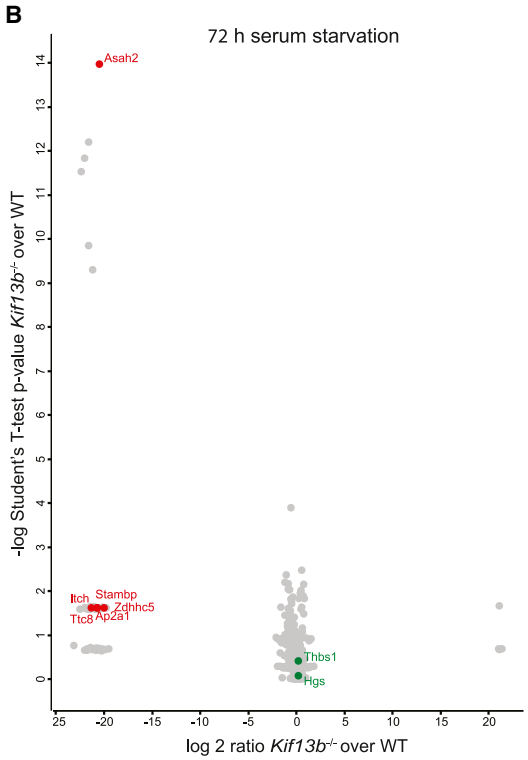

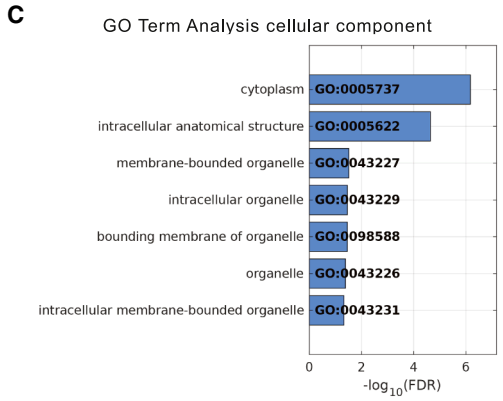

D

Abcg2, Acat2, Acot7, Aga, Aifm1, Ap2a1, Arhgap18, Arl4c, Arpc5, Asah1, **Asah2**, B2m, Ca2, Cdc42ep1, Cdca8, **Cnp**, **Crkl**, Dip2b, Ftl1;Ftl2, Glipr2, Gpd1l, Gpr126, Hnrnpa0, Hnrnpab, Homer3, **Itch**, Itfg3, Mme, Nras, **Ola1,** Pa2g4, **Pdap1**, Pfdn6, Phb2, **Plekhb2**, Rhob, Rpl10a, Rps18, Rtcb, Sec13, Serinc3, Srsf3, Stambp, **Tgm2**, Tmprss2, **Tnpo1**, Top1, Tra2b, Ttc8, **Usp6nl**, **Vamp3;Vamp2**, **Zdhhc5**

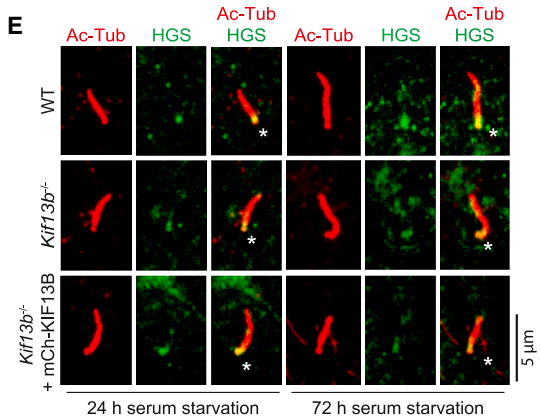

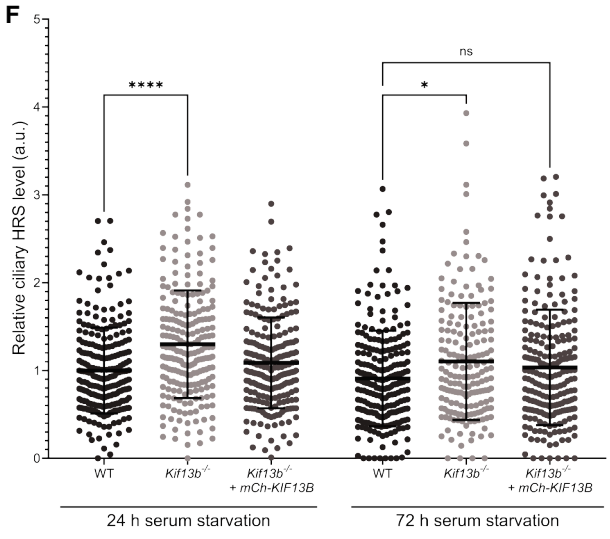

(legend on next page)

(Figure S5B). Similar results were obtained for WT and Kif13b$^{-/-}$ cells stably expressing mNG-ZDHHC5 (Figures S5C and S5D). Possibly, KIF13B affects both the targeting to and removal of ZDHHC5 from the cilium, leading to minimal effects of KIF13B loss on net ciliary ZDHHC5 levels.

To analyze the ciliary function of ZDHHC5, we knocked it out in mCCD cells (Figure 5C; Figures S5E and S5F) and analyzed WT and mutant cells by IFM for ciliary proteins. ZDHHC5 loss had little effect on ciliation frequency but caused a significant increase in ciliary length compared with WT (Figures 5D and 5E; Figure S5G). Furthermore, ciliary levels of PC2 were significantly decreased in the Zdhhc5$^{-/-}$ cells compared with WT, both after 24 and 72 h of starvation (Figures 5D and 5F), and total cellular PC2 levels were not lower in Zdhhc5$^{-/-}$ cells (Figure 5G). Thus, ciliary ZDHHC5 levels are negatively regulated by the BBSome, and ZDHHC5 loss causes ciliary lengthening and reduced ciliary PC2 content.

Loss of IFT27 alters ciliary content of HGS, FLOT1, ZDHHC5, and CCDC92

Previous work indicated that KIF13B accumulates in cilia of Ift27$^{-/-}$ IMCD3 cells.[67] Since IFT27 connects the BBSome to IFT trains during retrograde IFT,[68,69] we wondered if it functions upstream of KIF13B to regulate ciliary protein homeostasis. Supportively, IFM of WT and Ift27$^{-/-}$ IMCD3 cells showed that HGS and FLOT1 accumulate aberrantly within or at the base of cilia in Ift27$^{-/-}$ cells compared with WT (Figures S6A–S6D), and similar results were obtained for ZDHHC5 (Figures S6E–S6G). Moreover, CCDC92 was depleted from the ciliary tip of Ift27$^{-/-}$ cells (Figures S6H and S6I), as observed in 72 h serum-starved Kif13b$^{-/-}$ mCCD cells (Figures 2F and 2G). Thus, the Ift27$^{-/-}$ cells largely phenocopy the Kif13b$^{-/-}$ cells regarding ciliary localization of HGS, FLOT1, ZDHHC5, and CCDC92, supporting that IFT27 may function upstream of KIF13B in this context.

Altered ciliary PC2 levels upon treatment with endocytosis or ectocytosis inhibitors

The above-described results suggested that PC2 initially accumulates (24 h starvation) within Kif13b$^{-/-}$ cilia due to impaired HGS- and FLOT1-dependent endocytic retrieval and/or increased ciliary entrance owing to altered CCDC92/transition fiber function. After 72 h of starvation, accumulated PC2 may be shed from Kif13b$^{-/-}$ cilia in large EVs, causing its depletion from cilia. Consistent with this scenario, treatment of 24 h serum-starved WT cells with an endocytosis inhibitor (dynasore) or the CDC42 inhibitor ML141, which blocks EV release from cilia,[26] caused significant ciliary accumulation of PC2. Conversely, dynasore-treated Kif13b$^{-/-}$ cells showed a drop in the initial high ciliary PC2 content. A similar effect was observed for treatment with the nSMase2 inhibitor GW4869, whereas ML141 had little effect on ciliary PC2 levels in the mutant cells (Figures 6A–6E). These results support the conclusion that ciliary PC2 levels are downregulated by endocytic retrieval as well as EV release from cilia, and that these processes are regulated by KIF13B.

DISCUSSION

Our study shows that KIF13B regulates ciliary protein content and EV release in a time-dependent manner, as summarized in Figure 7. Newly formed Kif13b$^{-/-}$ cilia aberrantly accumulate PC2, FLOT1, and HGS (Figures 7A and 7B), but as cilia mature, this phenotype is reversed (Figures 7C and 7D). The alterations in ciliary protein content of Kif13b$^{-/-}$ cells are paralleled by changes in the overall release frequency and/or protein content of small and large EVs. Initially, KIF13B-deficient cells release fewer small EVs than WT cells, and such EVs are depleted for HGS, THBS1, and vimentin. Conversely, large EVs from 24 h serum-starved Kif13b$^{-/-}$ cells are enriched for CCDC198, CCDC92, and MLF2 but depleted for proteins like POFUT2 and DCTN6. Since PC2 was either absent (small EVs) or present in equal amounts (large EVs) in EV samples from 24 h serum-starved Kif13b$^{-/-}$ and WT cultures, we propose that PC2 initially accumulates within cilia of Kif13b$^{-/-}$ cells due to impaired HGS- and flotillin-dependent endocytic retrieval of PC2 from cilia, in line with our IFM results for dynasore-treated WT cells and the known role of HGS in ciliary PC2 homeostasis in *C. elegans*.[33] Alternatively, Kif13b$^{-/-}$ cells may have a leaky diffusion barrier at the ciliary base, leading to unrestricted ciliary entrance of PC2, HGS, and FLOT1 (Figure 7B). Indeed, we found that KIF13B retains CCDC92 at the ciliary base, with KIF13B loss causing CCDC92 to initially accumulate at the ciliary tip and then be released in large EVs. Similarly, enrichment of multiple ciliary proteins like PC2, BBSome, and IFT components in large EVs of 72 h serum-starved Kif13b$^{-/-}$ cells may be a compensatory response to their initial ciliary accumulation, explaining their depletion from cilia over time (Figures 7B and 7D). Consistently, aberrant accumulation of membrane-associated proteins in specific subcellular or ciliary compartments can trigger their EV release to promote organelle homeostasis,[22,30,31,70] and treatment with the CDC42 inhibitor ML141 that blocks EV release from cilia[26] conversely led to ciliary enrichment of PC2 in WT

Figure 4. Composition of small EVs

(A and B) Volcano plots comparing the protein content of small EVs from WT and Kif13b$^{-/-}$ cells after 24 h (A) and 72 h (B) of serum starvation, based on MS analysis (n = 4). Selected proteins differing significantly in abundance between mutant and WT samples (tier 1 or tier 2 hits) are in red, and proteins significantly altered at 24 h but not at 72 h are in green.

(C) GO Term Analysis for the category cellular component for proteins significantly altered in abundance in small EVs of Kif13b$^{-/-}$ cultures after 72 h. The tables show the GO terms that are significantly enriched (Fisher's exact test value $\leq$ 0.05), listed according to their enrichment ratio.

(D) List of proteins significantly altered in abundance in small EVs of Kif13b$^{-/-}$ cultures after 72 h (tier 1 and tier 2 hits). Proteins in bold accumulated in small EVs from *Bbs4* and/or *Bbs6* mutant KM cells.[19] Except for TGM2, all proteins listed were depleted from Kif13b$^{-/-}$ EVs.

(E) IFM of mCCD cells, stained for acetylated α-tubulin (AcTub) and HGS. Asterisk marks the ciliary base. mCh-KIF13B: mCherry-KIF13B.

(F) Quantification of relative ciliary HGS levels, based on images as in (E). 40–60 cilia were analyzed per cell line per experiment and normalized to WT 24 h mean value. Graphs show mean ± SD (n = 3), and significance was determined using the nonparametric Kruskal-Wallis test, followed by Dunn's multiple pairwise-comparison test.

See also Figures S3, S4, and S6 and Data S2A, S2B, and S3B.

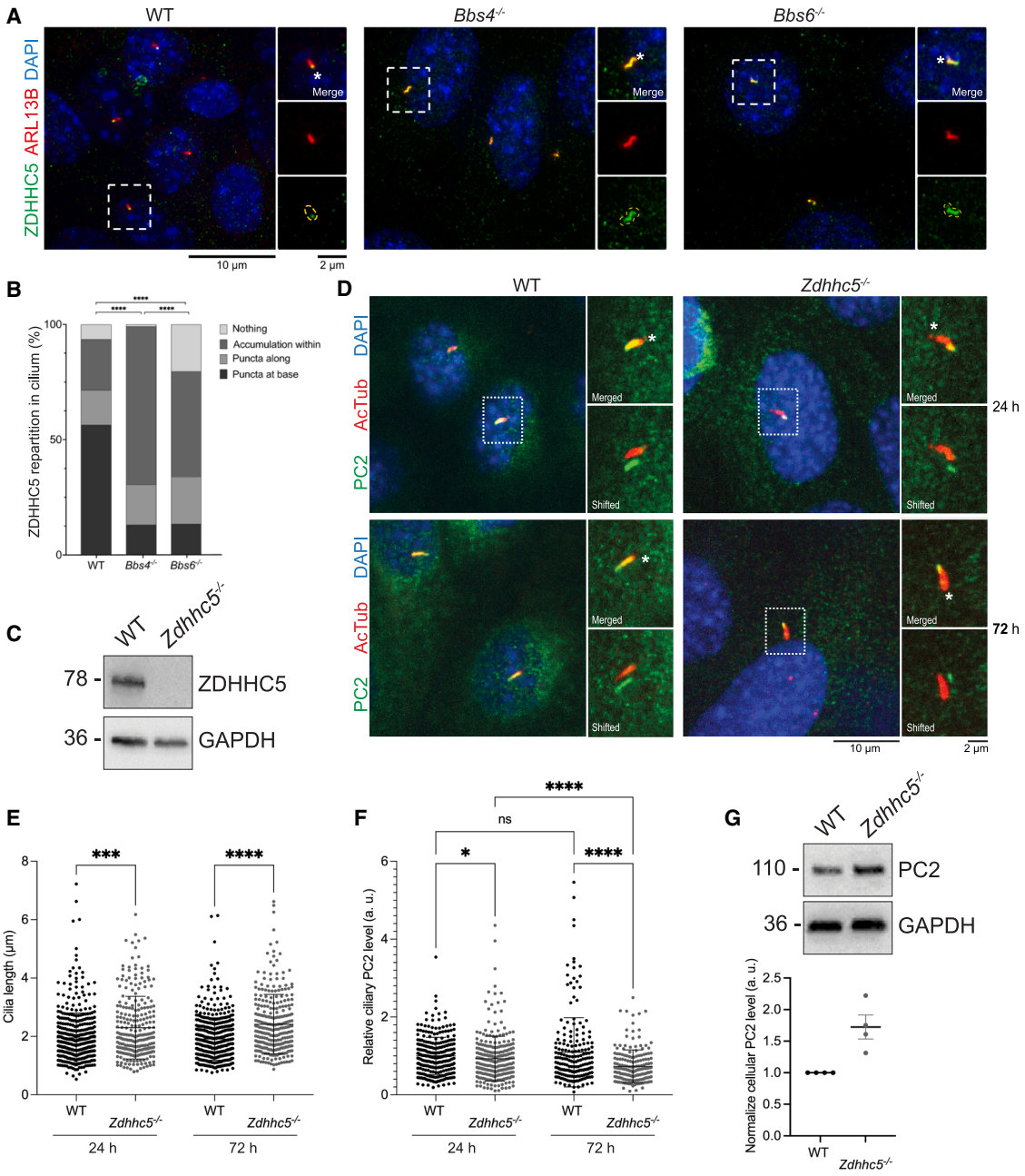

Figure 5. Ciliary localization and function of ZDHHC5

(A and B) IFM and quantitative analysis of ciliary staining intensities of 24 h serum-starved WT, *Bbs4*$^{-/-}$, and *Bbs6*$^{-/-}$ KM cells stained for ARL13B and ZDHHC5. DAPI marks nuclei. Insets show merged magnifications of selected cilia (boxed regions), and asterisk marks the ciliary base. In (B), a chi-squared test was used to test for contingency between sample distributions. Data represent the proportional distribution of each detected form of the ZDHHC5 staining.

(C and G) Western blot of WT and Zdhhc5$^{-/-}$ mCCD cells. GAPDH: loading control. Molecular mass markers are in kDa. The bottom panel in (G) shows quantitation of relative cellular levels of PC2. Graphs show mean ± SD (n = 4), and significance was determined using Wilcoxon signed-rank test.

(D) IFM of WT and Zdhhc5$^{-/-}$ mCCD cells, using indicated antibodies, and asterisk marks the ciliary base.

(E and F) Quantification of ciliary length (E) and relative ciliary PC2 intensity (F). CiliaQ[66] was used to measure ciliary length and PC2 MFI (n = 2) (see STAR Methods). Intensities were normalized to the mean ciliary PC2 MFI of WT. Graphs show mean ± SD, and significance was determined using an unpaired, two-tailed Student's t test.

See also Figures S5 and S6.

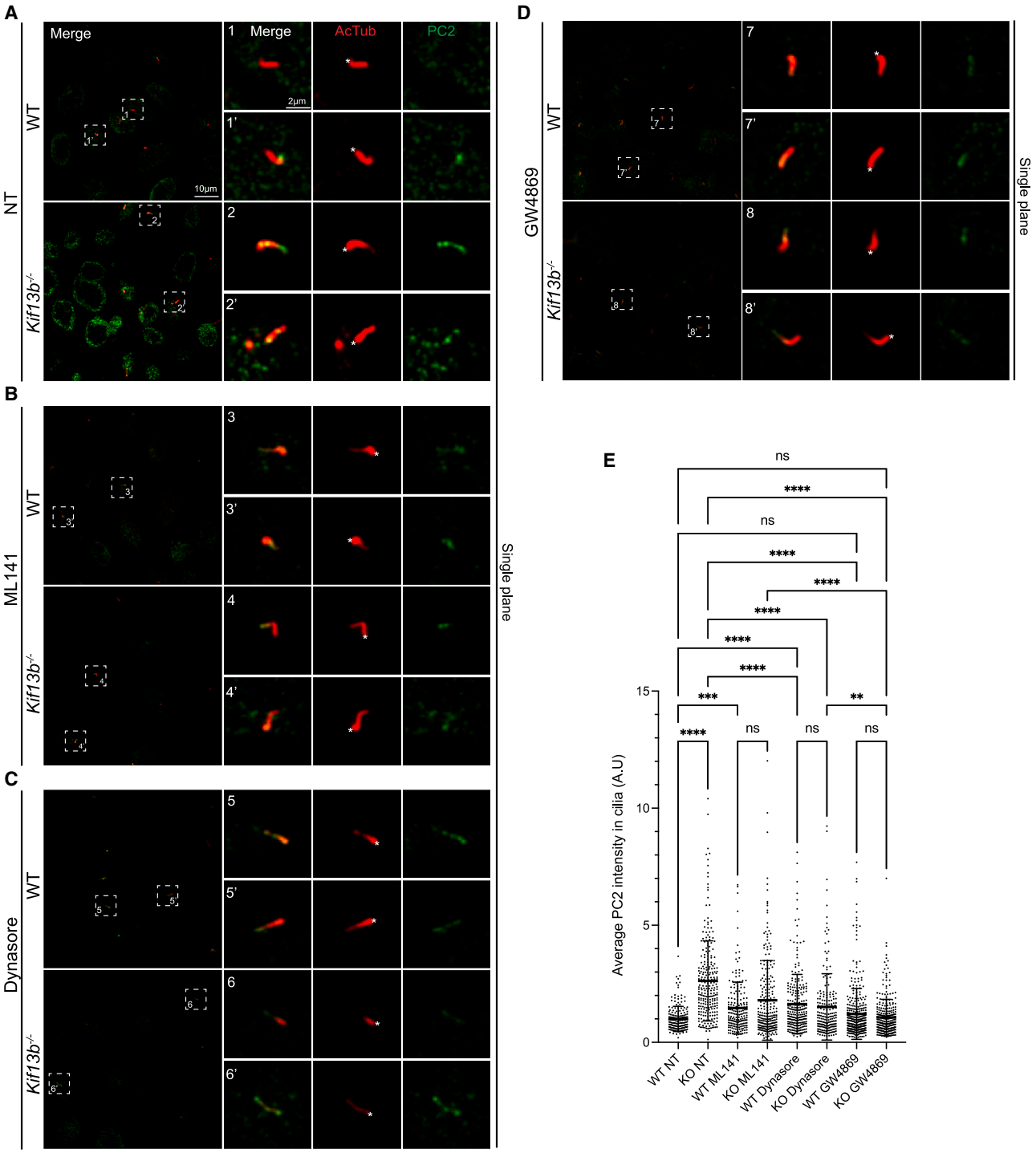

Figure 6. Effect of endocytosis and ectocytosis inhibitors on ciliary PC2 levels

(A–E) IFM and quantitative analysis of ciliary PC2 levels of 24 h serum-starved WT and Kif13b$^{-/-}$ cells without (NT) or with indicated drug treatment. Asterisk marks the ciliary base. For (E), quantitative analysis was done by a semi-automated approach and normalized to the mean ciliary MFI of WT NT PC2 level (n = 2). Knockout (KO) corresponds to Kif13b$^{-/-}$ cells. Statistical analysis: Kruskal-Wallis test.

cells. Thus, despite being localized to cilia and large EVs of mCCD cells, our results suggest that KIF13B suppresses the release of large EVs from cilia. This is unexpected since its homolog, KLP-6, promotes EV shedding from the ciliary tip of male sensory neurons in *C. elegans*, with loss of KLP-6 causing excessive shedding of EVs into the glial lumen encompassing the ciliary base.[35] Since it is unclear whether Kif13b$^{-/-}$ cells up-regulate large EV shedding from the tip or base of cilia, it remains

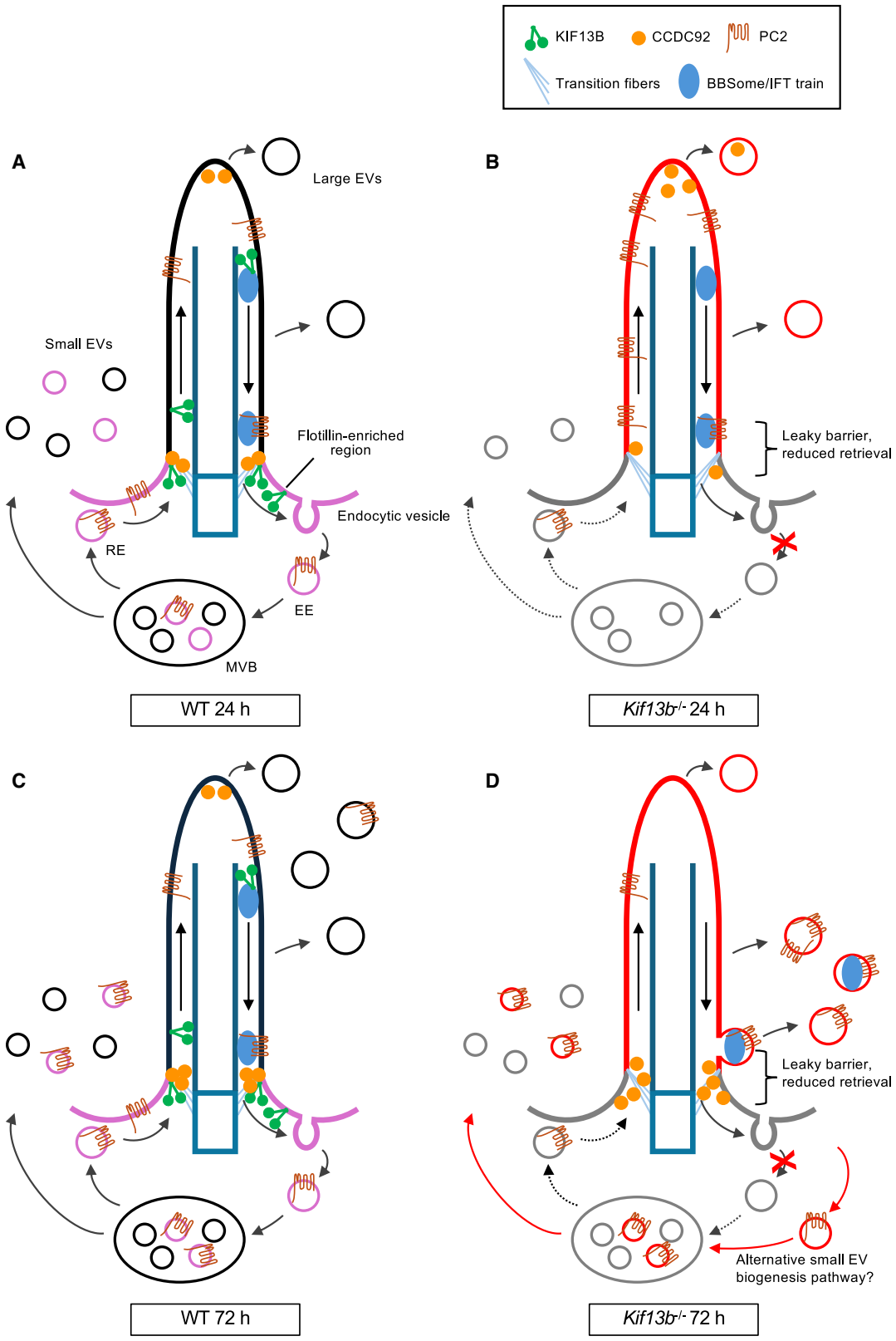

Figure 7. Summary of results and working model

(A) In 24 h serum-starved WT cells, KIF13B localizes dynamically along the cilium-basal body axis and is transported retrogradely by IFT.[41] PC2 is not released into large or small EVs, and CCDC92 localizes to the transition fibers and ciliary tip.

(legend continued on next page)

possible that PC2-containing large EVs are released from the ciliary base instead of the tip in these cells, as in *C. elegans klp-6* mutants. This would align with our observation that Kif13b$^{-/-}$ cilia display more membrane bulges along the side of cilia compared with WT cells, although by SEM, we only observe EVs that are just being budded, and not how many are actually being shed.

While numerous ciliary and non-ciliary proteins were altered in abundance in large and small EVs isolated from Kif13b$^{-/-}$ cells, reflecting the multiple cellular functions of KIF13B,[71,72] it is noteworthy that two out of three tier 1 proteins that accumulated within mutant large EVs at the 24 h time point (CCDC92 and CCDC198) localize to cilia. CCDC92 is a centriole DAP that binds CEP164[51] and is phosphorylated by TTBK2.[53] TTBK2 additionally binds CSNK2A1, and when *Csnk2a1* was knocked out in fibroblasts, cilia protein content was altered and EV release accelerated,[54] reminiscent of the Kif13b$^{-/-}$ phenotype. The authors also found that EVs from *Csnk2a1* mutant cells were enriched for FLOT1 and identified FLOT1, FLOT2, and CAV1 as proximity interactors of TTBK2.[54] This supports the notion that centriole DAPs may anchor to a specialized region of the periciliary membrane enriched for flotillins (and CAV1) and contribute to regulating EV biogenesis or endosomal trafficking associated with this region. Since KIF13B functions as a scaffold protein to regulate CAV1-mediated endocytosis[73] and CAV1 ciliary base localization,[40] it could modulate ciliary protein content at the level of transition fibers by regulating the interaction between DAPs and this specialized domain of the periciliary membrane (Figure 7). Although it remains unclear if KIF13B interacts physically with CCDC92 or other DAPs, we previously identified CSNK2A1 as a putative KIF13B interactor,[74] suggesting that KIF13B may affect DAP function via CSNK2A1. More work is needed to explore this possibility. Furthermore, while CCDC92 has previously been linked to cilia and DAPs,[51,53] its function at the cilium is unclear. Since several reports have linked CCDC92 to metabolic disorders like obesity and diabetes,[75–77] it will be interesting to explore if these phenotypes are linked to defects in ciliary function and/or EV release.

CCDC198 has not previously been shown to localize to cilia, but CCDC198 loss in mice caused altered body weight and decreased energy expenditure, correlating with genome-wide studies in humans linking CCDC198 to higher body mass index,[55] a common phenotype in ciliopathies.[2,3] CCDC198 localizes to the membrane of kidney epithelial cells and interacts directly with FNBP1L in a yeast two-hybrid screen.[55] As FNBP1L is a CDC42 effector that promotes actin-based endocytosis downstream of CDC42,[78] and activated CCDC42 triggers EV release from cilia,[26] KIF13B may promote release of CCDC198-containing EVs from cilia by a mechanism involving FNBP1L and CDC42. More work is needed to investigate this.

Apart from causing enrichment of ciliary proteins in large EVs after 72 h of starvation, KIF13B loss also substantially impacted small EV protein content at this time point. Specifically, Kif13b$^{-/-}$ small EVs lacked several proteins that were reported to be enriched in small EVs from BBSome-deficient KM cells,[19] including ZDHHC5, which we found localizes to cilia and regulates ciliary length and PC2 levels. Although ciliary levels of ZDHHC5 were largely unaffected by KIF13B loss, it accumulated within cilia of Ift27$^{-/-}$, *Bbs4*$^{-/-}$, and *Bbs6*$^{-/-}$ cells, supporting that the BBSome facilitates ciliary export of ZDHHC5 and that KIF13B may function downstream of the BBSome to promote its subsequent endocytic trafficking and small EV release. Notably, ZDHHC5 binds to DLG4,[79] a direct interactor of KIF13B,[80] suggesting that KIF13B may affect ZDHHC5 trafficking via DLG4 or its close homolog DLG1. Supportively, we recently showed that DLG1 loss causes PC2 depletion from cilia,[43] as observed for Zdhhc5$^{-/-}$ cells.

ZDHHC5 is a widely expressed protein that, among other processes, regulates synaptic plasticity, cardiac function, cell adhesion, and fatty acid uptake.[81] It has not previously been linked to cilia, but *Zdhhc5* knockout mice have phenotypes including short snout, reduced retinal thickness and fat tissue content, cardiac defects, and unilateral hydronephrosis.[82] Similar phenotypes are seen in ciliopathies,[2,3] warranting further investigations of *ZDHHC5* as a potential ciliopathy candidate gene.

RESOURCE AVAILABILITY

Lead contact

Requests for further information and resources should be directed to the lead contact, Lotte Bang Pedersen (lbpedersen@bio.ku.dk).

Materials availability

Cell lines and plasmids generated in this study are available from the lead contact without restriction.

Data and code availability

- Data: MS data have been deposited at MassIVE: MSV000098722 and ProteomeXchange: PXD066965.
- Code: this paper does not report original code.
- Additional information: any additional information required to reanalyze the data reported in this paper is available from the lead contact upon request.

ACKNOWLEDGMENTS

We thank Feng Qian and the Polycystic Kidney Disease Research Resource Consortium (U54DK126114) for the anti-PC2 antibody and Eric Féraille, Maxence Nachury, Kay Oliver Schink, Carlo Rivolta, Lukas Cajanek, and Yuko Mimori-Kiyosue for cell lines/reagents. We thank Geyi Li, Liva Karlshøj Julegaard, Emma Rose Jensen, Bjørk Ingeborg Bartholdy, Sandra Dieu Morsing, and Jannis von Spreckelsen for assistance with quantitative analysis of microscopy data and Sara Mesic, Jannis von Spreckelsen, Lotta Wagner, and Swaantje Hamdi for assistance with large EV characterization. We thank the staff of the Core Facility for Medical Proteomics, University of Tübingen for excellent support. This work was supported by grants NNF18SA0032928 and NNF22OC0080406 from the Novo Nordisk Foundation (L.B.P.), grant 2032-00115B from the Independent Research Fund Denmark (L.B.P.), the European Union's Horizon

(B) 24 h serum-starved Kif13b$^{-/-}$ cells accumulate PC2 (and HGS and FLOT1; not shown) in cilia, release fewer small EVs generated by the ceramide/nSMase2-dependent pathway, and show altered composition of both small and large EVs. This is due to a leaky diffusion barrier and impaired endocytic retrieval at the ciliary base, and CCDC92 redistributes from the ciliary base to the tip, where it is released in large EVs.
(C and D) 72 h serum-starved WT cells release PC2 in both large and small EVs. Large EV release of PC2 is increased in Kif13b$^{-/-}$ cells, causing ciliary PC2 depletion, and CCDC92 is lost from the ciliary tip due to its EV release and/or perturbed trafficking from the base to the tip. Kif13b$^{-/-}$ cells release small EVs devoid of cilia-derived proteins like ZDHHC5, which are generated by an nSMase2-independent pathway.

2020 research and innovation program Marie Sklodowska-Curie Innovative Training Networks (ITN) grant 861329 (L.B.P., S.T.C., and K.B.), the TheRaCil consortium funded by the European Union (Horizon-health-2022-disease-06-two stage, grant 101080717), and the Deutsche Forschungsgemeinschaft FOR5547, project ID MA 6139/6-1 503306912 (H.L.M.-S.).

AUTHOR CONTRIBUTIONS

C.K.R., A.F., F.C., A.M.F., A.-L.W.P., S.L.J., J.K.T.S., A.S., J.L., C.R.B., K.B., and Z.A. performed experiments; C.K.R., A.F., F.C., B.M., A.M.F., A.-L.W.P., C.R.B., K.B., M.C., H.L.M.-S., and Z.A. analyzed data; C.K.R., A.F., F.C., B.M., S.T.C., K.B., M.C., Z.A., H.L.M.-S., and L.B.P. prepared figures; M.W.B. supplied reagents; Z.A., H.L.M.-S., and L.B.P. conceived the project; L.B.P. wrote the paper with input from all authors; Z.A., S.T.C., K.B., H.L.M.-S., and L.B.P. obtained funding for the study.

DECLARATION OF INTERESTS

The authors declare no competing interests.

STAR★METHODS

Detailed methods are provided in the online version of this paper and include the following:

- KEY RESOURCES TABLE
- EXPERIMENTAL MODEL AND STUDY PARTICIPANT DETAILS
  - Cell lines and culture media
- METHOD DETAILS
  - Transfections and drug treatment
  - Gene knockout and rescue
  - SDS-PAGE and western blotting
  - Microscopy
  - Purification of extracellular vesicles
  - Nanoparticle tracking analysis (NTA)
  - Liquid chromatography (LC)-MS/MS analysis
- QUANTIFICATION AND STATISTICAL ANALYSIS
  - MS data analysis
  - GO term enrichment analysis
  - IFM and SEM data analysis
  - Western blot data analysis
  - NTA data analysis
  - Significance levels

SUPPLEMENTAL INFORMATION

Supplemental information can be found online at https://doi.org/10.1016/j.cub.2025.08.022.

Received: March 14, 2025
Revised: June 24, 2025
Accepted: August 12, 2025
Published: September 9, 2025

REFERENCES

1. Anvarian, Z., Mykytyn, K., Mukhopadhyay, S., Pedersen, L.B., and Christensen, S.T. (2019). Cellular signalling by primary cilia in development, organ function and disease. Nat. Rev. Nephrol. *15*, 199–219. https://doi.org/10.1038/s41581-019-0116-9.
2. Mill, P., Christensen, S.T., and Pedersen, L.B. (2023). Primary cilia as dynamic and diverse signalling hubs in development and disease. Nat. Rev. Genet. *24*, 421–441. https://doi.org/10.1038/s41576-023-00587-9.
3. Reiter, J.F., and Leroux, M.R. (2017). Genes and molecular pathways underpinning ciliopathies. Nat. Rev. Mol. Cell Biol. *18*, 533–547. https://doi.org/10.1038/nrm.2017.60.
4. Nachury, M.V., and Mick, D.U. (2019). Establishing and regulating the composition of cilia for signal transduction. Nat. Rev. Mol. Cell Biol. *20*, 389–405. https://doi.org/10.1038/s41580-019-0116-4.
5. Nguyen, T.D., Truong, M.E., and Reiter, J.F. (2022). The Intimate Connection Between Lipids and Hedgehog Signaling. Front. Cell Dev. Biol. *10*, 876815. https://doi.org/10.3389/fcell.2022.876815.
6. Hughes, J., Ward, C.J., Peral, B., Aspinwall, R., Clark, K., San Millán, J.L., Gamble, V., and Harris, P.C. (1995). The polycystic kidney disease 1 (PKD1) gene encodes a novel protein with multiple cell recognition domains. Nat. Genet. *10*, 151–160. https://doi.org/10.1038/ng0695-151.
7. Mochizuki, T., Wu, G., Hayashi, T., Xenophontos, S.L., Veldhuisen, B., Saris, J.J., Reynolds, D.M., Cai, Y., Gabow, P.A., Pierides, A., et al. (1996). PKD2, a Gene for Polycystic Kidney Disease That Encodes an Integral Membrane Protein. Science *272*, 1339–1342. https://doi.org/10.1126/science.272.5266.1339.
8. Yoder, B.K., Hou, X., and Guay-Woodford, L.M. (2002). The polycystic kidney disease proteins, polycystin-1, polycystin-2, polaris, and cystin, are co-localized in renal cilia. J. Am. Soc. Nephrol. *13*, 2508–2516. https://doi.org/10.1097/01.asn.0000029587.47950.25.
9. Pazour, G.J., San Agustin, J.T., Follit, J.A., Rosenbaum, J.L., and Witman, G.B. (2002). Polycystin-2 localizes to kidney cilia and the ciliary level is elevated in orpk mice with polycystic kidney disease. Curr. Biol. *12*, R378–R380. https://doi.org/10.1016/s0960-9822(02)00877-1.
10. Ma, M., Gallagher, A.R., and Somlo, S. (2017). Ciliary Mechanisms of Cyst Formation in Polycystic Kidney Disease. Cold Spring Harb. Perspect. Biol. *9*, a028209. https://doi.org/10.1101/cshperspect.a028209.
11. Hu, J., and Harris, P.C. (2020). Regulation of polycystin expression, maturation and trafficking. Cell. Signal. *72*, 109630. https://doi.org/10.1016/j.cellsig.2020.109630.
12. Luo, L., Roy, S., Li, L., and Ma, M. (2023). Polycystic kidney disease: novel insights into polycystin function. Trends Mol. Med. *29*, 268–281. https://doi.org/10.1016/j.molmed.2023.01.005.
13. Monis, W.J., Faundez, V., and Pazour, G.J. (2017). BLOC-1 is required for selective membrane protein trafficking from endosomes to primary cilia. J. Cell Biol. *216*, 2131–2150. https://doi.org/10.1083/jcb.201611138.
14. Walker, R.V., Keynton, J.L., Grimes, D.T., Sreekumar, V., Williams, D.J., Esapa, C., Wu, D., Knight, M.M., and Norris, D.P. (2019). Ciliary exclusion of Polycystin-2 promotes kidney cystogenesis in an autosomal dominant polycystic kidney disease model. Nat. Commun. *10*, 4072. https://doi.org/10.1038/s41467-019-12067-y.
15. van Niel, G., D'Angelo, G., and Raposo, G. (2018). Shedding light on the cell biology of extracellular vesicles. Nat. Rev. Mol. Cell Biol. *19*, 213–228. https://doi.org/10.1038/nrm.2017.125.
16. Dixson, A.C., Dawson, T.R., Di Vizio, D., and Weaver, A.M. (2023). Context-specific regulation of extracellular vesicle biogenesis and cargo selection. Nat. Rev. Mol. Cell Biol. *24*, 454–476. https://doi.org/10.1038/s41580-023-00576-0.
17. Wood, C.R., and Rosenbaum, J.L. (2015). Ciliary ectosomes: transmissions from the cell's antenna. Trends Cell Biol. *25*, 276–285. https://doi.org/10.1016/j.tcb.2014.12.008.
18. Akella, J.S., and Barr, M.M. (2021). The tubulin code specializes neuronal cilia for extracellular vesicle release. Dev. Neurobiol. *81*, 231–252. https://doi.org/10.1002/dneu.22787.
19. Volz, A.K., Frei, A., Kretschmer, V., de Jesus Domingues, A.M., Ketting, R.F., Ueffing, M., Boldt, K., Krämer-Albers, E.M., and May-Simera, H.L. (2021). Bardet-Biedl syndrome proteins modulate the release of bioactive extracellular vesicles. Nat. Commun. *12*, 5671. https://doi.org/10.1038/s41467-021-25929-1.
20. Ojeda Naharros, I., and Nachury, M.V. (2022). Shedding of ciliary vesicles at a glance. J. Cell Sci. *135*, jcs246553. https://doi.org/10.1242/jcs.246553.
21. Clupper, M., Gill, R., Elsayyid, M., Touroutine, D., Caplan, J.L., and Tanis, J.E. (2022). Kinesin-2 motors differentially impact biogenesis of

extracellular vesicle subpopulations shed from sensory cilia. iScience *25*, 105262. https://doi.org/10.1016/j.isci.2022.105262.

22. Nager, A.R., Goldstein, J.S., Herranz-Pérez, V., Portran, D., Ye, F., Garcia-Verdugo, J.M., and Nachury, M.V. (2017). An Actin Network Dispatches Ciliary GPCRs into Extracellular Vesicles to Modulate Signaling. Cell *168*, 252–263.e14. https://doi.org/10.1016/j.cell.2016.11.036.
23. Phua, S.C., Chiba, S., Suzuki, M., Su, E., Roberson, E.C., Pusapati, G.V., Setou, M., Rohatgi, R., Reiter, J.F., Ikegami, K., et al. (2017). Dynamic Remodeling of Membrane Composition Drives Cell Cycle through Primary Cilia Excision. Cell *168*, 264–279.e15. https://doi.org/10.1016/j.cell.2016.12.032.
24. Wang, G., Hu, H.B., Chang, Y., Huang, Y., Song, Z.Q., Zhou, S.B., Chen, L., Zhang, Y.C., Wu, M., Tu, H.Q., et al. (2019). Rab7 regulates primary cilia disassembly through cilia excision. J. Cell Biol. *218*, 4030–4041. https://doi.org/10.1083/jcb.201811136.
25. Stilling, S., Kalliakoudas, T., Benninghoven-Frey, H., Inoue, T., and Falkenburger, B.H. (2022). PIP(2) determines length and stability of primary cilia by balancing membrane turnovers. Commun. Biol. *5*, 93. https://doi.org/10.1038/s42003-022-03028-1.
26. Prasai, A., Ivashchenko, O., Maskova, K., Bykova, S., Schmidt Cernohorska, M., Stepanek, O., and Huranova, M. (2025). BBSome-deficient cells activate intraciliary CDC42 to trigger actin-dependent ciliary ectocytosis. EMBO Rep. *26*, 36–60. https://doi.org/10.1038/s44319-024-00326-z.
27. Nachury, M.V., Loktev, A.V., Zhang, Q., Westlake, C.J., Peränen, J., Merdes, A., Slusarski, D.C., Scheller, R.H., Bazan, J.F., Sheffield, V.C., et al. (2007). A core complex of BBS proteins cooperates with the GTPase Rab8 to promote ciliary membrane biogenesis. Cell *129*, 1201–1213. https://doi.org/10.1016/j.cell.2007.03.053.
28. Lechtreck, K.F., Johnson, E.C., Sakai, T., Cochran, D., Ballif, B.A., Rush, J., Pazour, G.J., Ikebe, M., and Witman, G.B. (2009). The Chlamydomonas reinhardtii BBSome is an IFT cargo required for export of specific signaling proteins from flagella. J. Cell Biol. *187*, 1117–1132. https://doi.org/10.1083/jcb.200909183.
29. Shinde, S.R., Nager, A.R., and Nachury, M.V. (2020). Ubiquitin chains earmark GPCRs for BBSome-mediated removal from cilia. J. Cell Biol. *219*, e202003020. https://doi.org/10.1083/jcb.202003020.
30. Akella, J.S., Carter, S.P., Nguyen, K., Tsiropoulou, S., Moran, A.L., Silva, M., Rizvi, F., Kennedy, B.N., Hall, D.H., Barr, M.M., et al. (2020). Ciliary Rab28 and the BBSome negatively regulate extracellular vesicle shedding. eLife *9*, e50580. https://doi.org/10.7554/eLife.50580.
31. Razzauti, A., and Laurent, P. (2021). Ectocytosis prevents accumulation of ciliary cargo in C. elegans sensory neurons. eLife *10*, e67670. https://doi.org/10.7554/eLife.67670.
32. Xu, Q., Zhang, Y., Wei, Q., Huang, Y., Li, Y., Ling, K., and Hu, J. (2015). BBS4 and BBS5 show functional redundancy in the BBSome to regulate the degradative sorting of ciliary sensory receptors. Sci. Rep. *5*, 11855. https://doi.org/10.1038/srep11855.
33. Hu, J., Wittekind, S.G., and Barr, M.M. (2007). STAM and Hrs down-regulate ciliary TRP receptors. Mol. Biol. Cell *18*, 3277–3289. https://doi.org/10.1091/mbc.E07-03-0239.
34. Scheidel, N., Kennedy, J., and Blacque, O.E. (2018). Endosome maturation factors Rabenosyn-5/VPS45 and caveolin-1 regulate ciliary membrane and polycystin-2 homeostasis. EMBO J. *37*, e98248. https://doi.org/10.15252/embj.201798248.
35. Wang, J., Silva, M., Haas, L.A., Morsci, N.S., Nguyen, K.C.Q., Hall, D.H., and Barr, M.M. (2014). C. elegans ciliated sensory neurons release extracellular vesicles that function in animal communication. Curr. Biol. *24*, 519–525. https://doi.org/10.1016/j.cub.2014.01.002.
36. Wood, C.R., Huang, K., Diener, D.R., and Rosenbaum, J.L. (2013). The cilium secretes bioactive ectosomes. Curr. Biol. *23*, 906–911. https://doi.org/10.1016/j.cub.2013.04.019.
37. Long, H., Zhang, F., Xu, N., Liu, G., Diener, D.R., Rosenbaum, J.L., and Huang, K. (2016). Comparative Analysis of Ciliary Membranes and Ectosomes. Curr. Biol. *26*, 3327–3335. https://doi.org/10.1016/j.cub.2016.09.055.
38. Hogan, M.C., Manganelli, L., Woollard, J.R., Masyuk, A.I., Masyuk, T.V., Tammachote, R., Huang, B.Q., Leontovich, A.A., Beito, T.G., Madden, B.J., et al. (2009). Characterization of PKD protein-positive exosome-like vesicles. J. Am. Soc. Nephrol. *20*, 278–288. https://doi.org/10.1681/ASN.2008060564.
39. Tanaka, Y., Morozumi, A., and Hirokawa, N. (2023). Nodal flow transfers polycystin to determine mouse left-right asymmetry. Dev. Cell *58*, 1447–1461.e6. https://doi.org/10.1016/j.devcel.2023.06.002.
40. Schou, K.B., Mogensen, J.B., Morthorst, S.K., Nielsen, B.S., Aleliunaite, A., Serra-Marques, A., Fürstenberg, N., Saunier, S., Bizet, A.A., Veland, I.R., et al. (2017). KIF13B establishes a CAV1-enriched microdomain at the ciliary transition zone to promote Sonic hedgehog signalling. Nat. Commun. *8*, 14177. https://doi.org/10.1038/ncomms14177.
41. Juhl, A.D., Anvarian, Z., Kuhns, S., Berges, J., Andersen, J.S., Wüstner, D., and Pedersen, L.B. (2023). Transient accumulation and bidirectional movement of KIF13B in primary cilia. J. Cell Sci. *136*, jcs259257. https://doi.org/10.1242/jcs.259257.
42. Montesano, R., Ghzili, H., Carrozzino, F., Rossier, B.C., and Féraille, E. (2009). cAMP-dependent chloride secretion mediates tubule enlargement and cyst formation by cultured mammalian collecting duct cells. Am. J. Physiol. Ren. Physiol. *296*, F446–F457. https://doi.org/10.1152/ajprenal.90415.2008.
43. Rezi, C.K., Aslanyan, M.G., Diwan, G.D., Cheng, T., Chamlali, M., Junger, K., Anvarian, Z., Lorentzen, E., Pauly, K.B., Afshar-Bahadori, Y., et al. (2024). DLG1 functions upstream of SDCCAG3 and IFT20 to control ciliary targeting of polycystin-2. EMBO Rep. *25*, 3040–3063. https://doi.org/10.1038/s44319-024-00170-1.
44. He, K., Ma, X., Xu, T., Li, Y., Hodge, A., Zhang, Q., Torline, J., Huang, Y., Zhao, J., Ling, K., et al. (2018). Axoneme polyglutamylation regulated by Joubert syndrome protein ARL13B controls ciliary targeting of signaling molecules. Nat. Commun. *9*, 3310. https://doi.org/10.1038/s41467-018-05867-1.
45. Dubreuil, V., Marzesco, A.M., Corbeil, D., Huttner, W.B., and Wilsch-Bräuninger, M. (2007). Midbody and primary cilium of neural progenitors release extracellular membrane particles enriched in the stem cell marker prominin-1. J. Cell Biol. *176*, 483–495. https://doi.org/10.1083/jcb.200608137.
46. Chacon-Heszele, M.F., Choi, S.Y., Zuo, X., Baek, J.I., Ward, C., and Lipschutz, J.H. (2014). The exocyst and regulatory GTPases in urinary exosomes. Physiol. Rep. *2*, e12116. https://doi.org/10.14814/phy2.12116.
47. Huang, F., Sirinakis, G., Allgeyer, E.S., Schroeder, L.K., Duim, W.C., Kromann, E.B., Phan, T., Rivera-Molina, F.E., Myers, J.R., Irnov, I., et al. (2016). Ultra-High Resolution 3D Imaging of Whole Cells. Cell *166*, 1028–1040. https://doi.org/10.1016/j.cell.2016.06.016.
48. Sun, S., Fisher, R.L., Bowser, S.S., Pentecost, B.T., and Sui, H. (2019). Three-dimensional architecture of epithelial primary cilia. Proc. Natl. Acad. Sci. USA *116*, 9370–9379. https://doi.org/10.1073/pnas.1821064116.
49. Kiesel, P., Alvarez Viar, G., Tsoy, N., Maraspini, R., Gorilak, P., Varga, V., Honigmann, A., and Pigino, G. (2020). The molecular structure of mammalian primary cilia revealed by cryo-electron tomography. Nat. Struct. Mol. Biol. *27*, 1115–1124. https://doi.org/10.1038/s41594-020-0507-4.
50. Samsonov, R., Shtam, T., Burdakov, V., Glotov, A., Tsyrlina, E., Berstein, L., Nosov, A., Evtushenko, V., Filatov, M., and Malek, A. (2016). Lectin-induced agglutination method of urinary exosomes isolation followed by mi-RNA analysis: Application for prostate cancer diagnostic. Prostate *76*, 68–79. https://doi.org/10.1002/pros.23101.
51. Chaki, M., Airik, R., Ghosh, A.K., Giles, R.H., Chen, R., Slaats, G.G., Wang, H., Hurd, T.W., Zhou, W., Cluckey, A., et al. (2012). Exome capture reveals ZNF423 and CEP164 mutations, linking renal ciliopathies to DNA damage response signaling. Cell *150*, 533–548. https://doi.org/10.1016/j.cell.2012.06.028.

52. Goetz, S.C., Liem, K.F., Jr., and Anderson, K.V. (2012). The spinocerebellar ataxia-associated gene Tau tubulin kinase 2 controls the initiation of ciliogenesis. Cell *151*, 847–858. https://doi.org/10.1016/j.cell.2012.10.010.

53. Bernatik, O., Pejskova, P., Vyslouzil, D., Hanakova, K., Zdrahal, Z., and Cajanek, L. (2020). Phosphorylation of multiple proteins involved in ciliogenesis by Tau Tubulin kinase 2. Mol. Biol. Cell *31*, 1032–1046. https://doi.org/10.1091/mbc.E19-06-0334.

54. Loukil, A., Barrington, C., and Goetz, S.C. (2021). A complex of distal appendage-associated kinases linked to human disease regulates ciliary trafficking and stability. Proc. Natl. Acad. Sci. USA *118*, e2018740118. https://doi.org/10.1073/pnas.2018740118.

55. Petersen, J., Englmaier, L., Artemov, A.V., Poverennaya, I., Mahmoud, R., Bouderlique, T., Tesarova, M., Deviatiiarov, R., Szilvásy-Szabó, A., Akkuratov, E.E., et al. (2023). A previously uncharacterized Factor Associated with Metabolism and Energy (FAME/C14orf105/CCDC198/1700011H14Rik) is related to evolutionary adaptation, energy balance, and kidney physiology. Nat. Commun. *14*, 3092. https://doi.org/10.1038/s41467-023-38663-7.

56. He, Q., Wang, G., Wakade, S., Dasgupta, S., Dinkins, M., Kong, J.N., Spassieva, S.D., and Bieberich, E. (2014). Primary cilia in stem cells and neural progenitors are regulated by neutral sphingomyelinase 2 and ceramide. Mol. Biol. Cell *25*, 1715–1729. https://doi.org/10.1091/mbc.E13-12-0730.

57. Wu, D., Huang, J., Zhu, H., Chen, Z., Chai, Y., Ke, J., Lei, K., Peng, Z., Zhang, R., Li, X., et al. (2022). Ciliogenesis requires sphingolipid-dependent membrane and axoneme interaction. Proc. Natl. Acad. Sci. USA *119*, e2201096119. https://doi.org/10.1073/pnas.2201096119.

58. Kundu, S., Rohokale, R., Lin, C., Chen, S., Biswas, S., and Guo, Z. (2024). Bifunctional glycosphingolipid (GSL) probes to investigate GSL-interacting proteins in cell membranes. J. Lipid Res. *65*, 100570. https://doi.org/10.1016/j.jlr.2024.100570.

59. Jerman, S., Ward, H.H., Lee, R., Lopes, C.A.M., Fry, A.M., MacDougall, M., and Wandinger-Ness, A. (2014). OFD1 and flotillins are integral components of a ciliary signaling protein complex organized by polycystins in renal epithelia and odontoblasts. PLoS One *9*, e106330. https://doi.org/10.1371/journal.pone.0106330.

60. Ansley, S.J., Badano, J.L., Blacque, O.E., Hill, J., Hoskins, B.E., Leitch, C.C., Kim, J.C., Ross, A.J., Eichers, E.R., Teslovich, T.M., et al. (2003). Basal body dysfunction is a likely cause of pleiotropic Bardet-Biedl syndrome. Nature *425*, 628–633. https://doi.org/10.1038/nature02030.

61. Wright, M.H., Berlin, I., and Nash, P.D. (2011). Regulation of endocytic sorting by ESCRT-DUB-mediated deubiquitination. Cell Biochem. Biophys. *60*, 39–46. https://doi.org/10.1007/s12013-011-9181-9.

62. O'Connor, H.F., Lyon, N., Leung, J.W., Agarwal, P., Swaim, C.D., Miller, K.M., and Huibregtse, J.M. (2015). Ubiquitin-Activated Interaction Traps (UBAITs) identify E3 ligase binding partners. EMBO Rep. *16*, 1699–1712. https://doi.org/10.15252/embr.201540620.

63. Kohli, P., Höhne, M., Jüngst, C., Bertsch, S., Ebert, L.K., Schauss, A.C., Benzing, T., Rinschen, M.M., and Schermer, B. (2017). The ciliary membrane-associated proteome reveals actin-binding proteins as key components of cilia. EMBO Rep. *18*, 1521–1535. https://doi.org/10.15252/embr.201643846.

64. Meister, M., Bänfer, S., Gärtner, U., Koskimies, J., Amaddii, M., Jacob, R., and Tikkanen, R. (2017). Regulation of cargo transfer between ESCRT-0 and ESCRT-I complexes by flotillin-1 during endosomal sorting of ubiquitinated cargo. Oncogenesis *6*, e344. https://doi.org/10.1038/oncsis.2017.47.

65. Li, Y., Martin, B.R., Cravatt, B.F., and Hofmann, S.L. (2012). DHHC5 protein palmitoylates flotillin-2 and is rapidly degraded on induction of neuronal differentiation in cultured cells. J. Biol. Chem. *287*, 523–530. https://doi.org/10.1074/jbc.M111.306183.

66. Hansen, J.N., Rassmann, S., Stuven, B., Jurisch-Yaksi, N., and Wachten, D. (2021). CiliaQ: a simple, open-source software for automated quantification of ciliary morphology and fluorescence in 2D, 3D, and 4D images. Eur. Phys. J. E Soft Matter *44*, 18. https://doi.org/10.1140/epje/s10189-021-00031-y.

67. Mick, D.U., Rodrigues, R.B., Leib, R.D., Adams, C.M., Chien, A.S., Gygi, S.P., and Nachury, M.V. (2015). Proteomics of Primary Cilia by Proximity Labeling. Dev. Cell *35*, 497–512. https://doi.org/10.1016/j.devcel.2015.10.015.

68. Eguether, T., San Agustin, J.T., Keady, B.T., Jonassen, J.A., Liang, Y., Francis, R., Tobita, K., Johnson, C.A., Abdelhamed, Z.A., Lo, C.W., et al. (2014). IFT27 links the BBSome to IFT for maintenance of the ciliary signaling compartment. Dev. Cell *31*, 279–290. https://doi.org/10.1016/j.devcel.2014.09.011.

69. Liew, G.M., Ye, F., Nager, A.R., Murphy, J.P., Lee, J.S., Aguiar, M., Breslow, D.K., Gygi, S.P., and Nachury, M.V. (2014). The Intraflagellar Transport Protein IFT27 Promotes BBSome Exit from Cilia through the GTPase ARL6/BBS3. Dev. Cell *31*, 265–278. https://doi.org/10.1016/j.devcel.2014.09.004.

70. Lewis, T.R., Castillo, C.M., Klementieva, N.V., Hsu, Y., Hao, Y., Spencer, W.J., Drack, A.V., Pazour, G.J., and Arshavsky, V.Y. (2024). Contribution of intraflagellar transport to compartmentalization and maintenance of the photoreceptor cell. Proc. Natl. Acad. Sci. USA *121*, e2408551121. https://doi.org/10.1073/pnas.2408551121.

71. Siddiqui, N., and Straube, A. (2017). Intracellular Cargo Transport by Kinesin-3 Motors. Biochemistry (Mosc) *82*, 803–815. https://doi.org/10.1134/S0006297917070057.

72. Morthorst, S.K., Christensen, S.T., and Pedersen, L.B. (2018). Regulation of ciliary membrane protein trafficking and signalling by kinesin motor proteins. FEBS J. *285*, 4535–4564. https://doi.org/10.1111/febs.14583.

73. Kanai, Y., Wang, D., and Hirokawa, N. (2014). KIF13B enhances the endocytosis of LRP1 by recruiting LRP1 to caveolae. J. Cell Biol. *204*, 395–408. https://doi.org/10.1083/jcb.201309066.

74. Morthorst, S.K., Nielsen, C., Farinelli, P., Anvarian, Z., Rasmussen, C.B.R., Serra-Marques, A., Grigoriev, I., Altelaar, M., Fürstenberg, N., Ludwig, A., et al. (2022). Angiomotin isoform 2 promotes binding of PALS1 to KIF13B at primary cilia and regulates ciliary length and signaling. J. Cell Sci. *135*, jcs259471. https://doi.org/10.1242/jcs.259471.

75. Huang, L.O., Rauch, A., Mazzaferro, E., Preuss, M., Carobbio, S., Bayrak, C.S., Chami, N., Wang, Z., Schick, U.M., Yang, N., et al. (2021). Genome-wide discovery of genetic loci that uncouple excess adiposity from its comorbidities. Nat. Metab. *3*, 228–243. https://doi.org/10.1038/s42255-021-00346-2.

76. Ren, L., Du, W., Song, D., Lu, H., Hamblin, M.H., Wang, C., Du, C., Fan, G.C., Becker, R.C., and Fan, Y. (2023). Genetic ablation of diabetes-associated gene Ccdc92 reduces obesity and insulin resistance in mice. iScience *26*, 105769. https://doi.org/10.1016/j.isci.2022.105769.

77. Zuo, F., Wang, Y., Xu, X., Ding, R., Tang, W., Sun, Y., Wang, X., Zhang, Y., Wu, J., Xie, Y., et al. (2024). CCDC92 deficiency ameliorates podocyte lipotoxicity in diabetic kidney disease. Metabolism *150*, 155724. https://doi.org/10.1016/j.metabol.2023.155724.

78. Ho, H.Y.H., Rohatgi, R., Lebensohn, A.M., Le, M., Li, J., Gygi, S.P., and Kirschner, M.W. (2004). Toca-1 mediates Cdc42-dependent actin nucleation by activating the N-WASP-WIP complex. Cell *118*, 203–216. https://doi.org/10.1016/j.cell.2004.06.027.

79. Brigidi, G.S., Santyr, B., Shimell, J., Jovellar, B., and Bamji, S.X. (2015). Activity-regulated trafficking of the palmitoyl-acyl transferase DHHC5. Nat. Commun. *6*, 8200. https://doi.org/10.1038/ncomms9200.

80. Zhu, J., Shang, Y., Xia, Y., Zhang, R., and Zhang, M. (2016). An Atypical MAGUK GK Target Recognition Mode Revealed by the Interaction between DLG and KIF13B. Structure *24*, 1876–1885. https://doi.org/10.1016/j.str.2016.08.008.

81. Woodley, K.T., and Collins, M.O. (2021). Regulation and function of the palmitoyl-acyltransferase ZDHHC5. FEBS J. *288*, 6623–6634. https://doi.org/10.1111/febs.15709.

82. da Silva-Buttkus, P., Spielmann, N., Klein-Rodewald, T., Schütt, C., Aguilar-Pimentel, A., Amarie, O.V., Becker, L., Calzada-Wack, J., Garrett, L., Gerlini,

R., et al. (2023). Knockout mouse models as a resource for the study of rare diseases. Mamm. Genome *34*, 244–261. https://doi.org/10.1007/s00335-023-09986-z.

83. Ashburner, M., Ball, C.A., Blake, J.A., Botstein, D., Butler, H., Cherry, J.M., Davis, A.P., Dolinski, K., Dwight, S.S., Eppig, J.T., et al. (2000). Gene ontology: tool for the unification of biology. The Gene Ontology Consortium. Nat. Genet. *25*, 25–29. https://doi.org/10.1038/75556.
84. the Gene Ontology Consortium (2017). Expansion of the Gene Ontology knowledgebase and resources. Nucleic Acids Res. *45*, D331–D338. https://doi.org/10.1093/nar/gkw1108.
85. Hernandez-Hernandez, V., Pravincumar, P., Diaz-Font, A., May-Simera, H., Jenkins, D., Knight, M., and Beales, P.L. (2013). Bardet-Biedl syndrome proteins control the cilia length through regulation of actin polymerization. Hum. Mol. Genet. *22*, 3858–3868. https://doi.org/10.1093/hmg/ddt241.
86. Lamason, R.L., Kupfer, A., and Pomerantz, J.L. (2010). The dynamic distribution of CARD11 at the immunological synapse is regulated by the inhibitory kinesin GAKIN. Mol. Cell *40*, 798–809. https://doi.org/10.1016/j.molcel.2010.11.007.
87. Tian, H., Lu, J.Y., Shao, C., Huffman, K.E., Carstens, R.M., Larsen, J.E., Girard, L., Liu, H., Rodriguez-Canales, J., Frenkel, E.P., et al. (2015). Systematic siRNA Screen Unmasks NSCLC Growth Dependence by Palmitoyltransferase DHHC5. Mol. Cancer Res. *13*, 784–794. https://doi.org/10.1158/1541-7786.MCR-14-0608.
88. Ran, F.A., Hsu, P.D., Wright, J., Agarwala, V., Scott, D.A., and Zhang, F. (2013). Genome engineering using the CRISPR-Cas9 system. Nat. Protoc. *8*, 2281–2308. https://doi.org/10.1038/nprot.2013.143.
89. Campeau, E., Ruhl, V.E., Rodier, F., Smith, C.L., Rahmberg, B.L., Fuss, J.O., Campisi, J., Yaswen, P., Cooper, P.K., and Kaufman, P.D. (2009). A versatile viral system for expression and depletion of proteins in mammalian cells. PLoS One *4*, e6529. https://doi.org/10.1371/journal.pone.0006529.
90. Schindelin, J., Arganda-Carreras, I., Frise, E., Kaynig, V., Longair, M., Pietzsch, T., Preibisch, S., Rueden, C., Saalfeld, S., Schmid, B., et al. (2012). Fiji: an open-source platform for biological-image analysis. Nat. Methods *9*, 676–682. https://doi.org/10.1038/nmeth.2019.
91. Demichev, V., Messner, C.B., Vernardis, S.I., Lilley, K.S., and Ralser, M. (2020). DIA-NN: neural networks and interference correction enable deep proteome coverage in high throughput. Nat. Methods *17*, 41–44. https://doi.org/10.1038/s41592-019-0638-x.
92. Cox, J., and Mann, M. (2008). MaxQuant enables high peptide identification rates, individualized p.p.b.-range mass accuracies and proteome-wide protein quantification. Nat. Biotechnol. *26*, 1367–1372. https://doi.org/10.1038/nbt.1511.
93. Thomas, P.D., Ebert, D., Muruganujan, A., Mushayahama, T., Albou, L.P., and Mi, H. (2022). PANTHER: Making genome-scale phylogenetics accessible to all. Protein Sci. *31*, 8–22. https://doi.org/10.1002/pro.4218.
94. Tyanova, S., Temu, T., Sinitcyn, P., Carlson, A., Hein, M.Y., Geiger, T., Mann, M., and Cox, J. (2016). The Perseus computational platform for comprehensive analysis of (prote)omics data. Nat. Methods *13*, 731–740. https://doi.org/10.1038/nmeth.3901.
95. Doench, J.G., Fusi, N., Sullender, M., Hegde, M., Vaimberg, E.W., Donovan, K.F., Smith, I., Tothova, Z., Wilen, C., Orchard, R., et al. (2016). Optimized sgRNA design to maximize activity and minimize off-target effects of CRISPR-Cas9. Nat. Biotechnol. *34*, 184–191. https://doi.org/10.1038/nbt.3437.
96. Aslanyan, M.G., Doornbos, C., Diwan, G.D., Anvarian, Z., Beyer, T., Junger, K., van Beersum, S.E.C., Russell, R.B., Ueffing, M., Ludwig, A., et al. (2023). A targeted multi-proteomics approach generates a blueprint of the ciliary ubiquitinome. Front. Cell Dev. Biol. *11*, 1113656. https://doi.org/10.3389/fcell.2023.1113656.
97. Hua, K., and Ferland, R.J. (2017). Fixation methods can differentially affect ciliary protein immunolabeling. Cilia *6*, 5. https://doi.org/10.1186/s13630-017-0045-9.
98. Meier, F., Brunner, A.D., Frank, M., Ha, A., Bludau, I., Voytik, E., Kaspar-Schoenefeld, S., Lubeck, M., Raether, O., Bache, N., et al. (2020). diaPASEF: parallel accumulation-serial fragmentation combined with data-independent acquisition. Nat. Methods *17*, 1229–1236. https://doi.org/10.1038/s41592-020-00998-0.
99. Cox, J., Hein, M.Y., Luber, C.A., Paron, I., Nagaraj, N., and Mann, M. (2014). Accurate proteome-wide label-free quantification by delayed normalization and maximal peptide ratio extraction, termed MaxLFQ. Mol. Cell. Proteomics *13*, 2513–2526. https://doi.org/10.1074/mcp.M113.031591.

STAR★METHODS

KEY RESOURCES TABLE

REAGENT or RESOURCE	SOURCE	IDENTIFIER
Antibodies		
Acetylated alpha-tubulin (mouse monoclonal)	Sigma-Aldrich	Cat# T7451; RRID: AB_609894
Acetylated alpha-tubulin (rabbit monoclonal)	Abcam	Cat# ab179484; RRID: AB_2890906
AIP1/ALIX (mouse monoclonal)	BD Biosciences	Cat# 611620; RRID: AB_399062
AIP1/ALIX (rabbit polyclonal)	Sigma-Aldrich	Cat# ABC40 RRID: AB_10806218
Alexa Fluor™ 350 Donkey anti-Rabbit IgG (H+L) Highly Cross-Adsorbed Secondary Antibody	Invitrogen	Cat# A10039
Alexa Fluor™ 488 Donkey anti-Mouse IgG (H+L) Highly Cross-Adsorbed Secondary Antibody	Invitrogen	Cat# A-21202
Alexa Fluor™ 488 Donkey anti-Rabbit IgG (H+L) Highly Cross-Adsorbed Secondary Antibody	Invitrogen	Cat# A-21206
Alexa Fluor™ 568 Donkey anti-Mouse IgG (H+L) Highly Cross-Adsorbed Secondary Antibody	Invitrogen	Cat #A10037
Alexa Fluor™ 568 Donkey anti-Rabbit IgG (H+L) Highly Cross-Adsorbed Secondary Antibody	Invitrogen	Cat #A10042
Alexa Fluor™ 647 Goat anti-Guinea Pig IgG (H+L) Highly Cross-Adsorbed Secondary Antibody	Invitrogen	Cat# A-21450
Alpha-tubulin (mouse monoclonal)	Sigma-Aldrich	Cat# T5168; RRID: AB_477579
ARF6 (rabbit polyclonal)	Abcam	Cat# ab77581; RRID: AB_2058475
ARL13B (rabbit polyclonal)	Proteintech	Cat# 17711-1-AP; RRID: AB_2060867
ARL13B N295B/66 (mouse polyclonal)	Abcam	Cat# ab136648; RRID: AB_3073658
ARL13B (guinea pig)	Proteintech	Cat# 30332-1-AP; RRID: AB_3086296
CCDC92 (rabbit polyclonal)	Proteintech	Cat# 27192-1-AP; RRID: AB_2880794
CCDC198 (mouse monoclonal)	Santa Cruz Biotechnology	Cat# sc-398907
CD81 (mouse monoclonal)	Santa Cruz Biotechnology	Cat# sc-166029; RRID: AB_2275892
CD9 (rat monoclonal)	BD Biosciences	Cat# 553758; RRID: AB_395032
CEP164 (rabbit polyclonal)	Sigma-Aldrich	Cat# HPA037606; RRID: AB_10672498
FLAG (mouse monoclonal)	Sigma-Aldrich	Cat# F1804; RRID: AB_262044
FLOT1 (rabbit polyclonal)	Sigma-Aldrich	Cat# F1180; RRID: AB_1078893
FLOT1 (goat polyclonal)	Abcam	Cat# ab13493; RRID: AB_2294271
GAPDH (rabbit recombinant monoclonal)	Cell Signalling Technology	Cat# 2118; RRID: AB_561053
GM130 (mouse monoclonal)	BD Biosciences	Cat# 610823; RRID: AB_398142
HGS (rabbit polyclonal)	Proteintech	Cat# 10390-1-AP; RRID: AB_2118914
HSP70 (mouse monoclonal)	BD Biosciences	Cat# 610608; RRID: AB_397942
KIF13B (mouse monoclonal)	Sigma-Aldrich	Cat# SAB1412812
IRDye 680RD Donkey anti-Mouse IgG	LI-COR Bioscience	Cat# 925-68072; RRID: AB_2814912
IRDye 800CW Donkey anti-Mouse IgG	LI-COR Bioscience	Cat# 925-32212; RRID: AB_2716622
Polyclonal Goat Anti-Mouse Immunoglobulins/HRP	Dako	Cat# P0447
Polyclonal Rabbit Anti-Goat Immunoglobulins/HRP	Dako	Cat# P0449
Polyclonal Rabbit Anti-Rat Immunoglobulins/HRP	Dako	Cat# P0450
Polyclonal Swine Anti-Rabbit Immunoglobulins/HRP	Dako	Cat# P0399
Polycystin-2 (rabbit polyclonal)	PKD Research Resource Consortium	N/A
Polycystin-2 (D-3) (mouse monoclonal)	Santa Cruz	Cat# sc-28331; RRID: AB_672377
IRDye 680RD Donkey anti-Rabbit IgG	LI-COR Bioscience	Cat# 925-68073; RRID: AB_2716687

(*Continued on next page*)

Continued

REAGENT or RESOURCE	SOURCE	IDENTIFIER
Goat anti-Rat IgG (H+L) Cross-Adsorbed Secondary Antibody, Alexa Fluor™ 680	Thermo Fisher Scientific	Cat# A-21096; RRID: AB_2535750
RPGRIP1L (guinea pig)	Eurogentec	Cat# snc039
TSG101 (mouse monoclonal)	Gene Tex	Cat# GTX70255; RRID: AB_373239
ZDHHC5 (rabbit polyclonal)	Proteintech	Cat# 21324-1-AP; RRID: AB_10732816
Bacterial and virus strains		
Escherichia coli DH10B	Lab stock	N/A
Chemicals, peptides, and recombinant proteins		
Acetonitril (LC-MS-grade, Chromasolv)	Sigma-Aldrich	Cat# 349672.5L
Blasticidin	Gibco	Cat# r210-01
Concanavalin A from *Canavalia ensiformis*	Sigma-Aldrich	Cat# C2010
Dexamethasone	Merck	Cat# D4902
1,4-Dithiothreitol	Millipore	Cat# 1.11474.0025
Dynasore	Sigma-Aldrich	Cat# D7693
EGF	Merck	Cat# SRP3196
Formic acid, 99.0%, Optima, LC-MS grade	Fisher Scientific	Cat# A11750
GW4869	Sigma-Aldrich	Cat# D1692
Holo-transferrin	Merck	Cat# T0665
Insulin	Merck	Cat# I6634
2-Iodacetamide	Merck	Cat# 8.04744.0025
Lipofectamine 3000	Thermo Fisher Scientific	Cat# L3000015
ML141	Tocris	Cat# 4266
NuPAGE™ LDS Sample Buffer (4X)	Thermo Fischer Scientific	Cat# NP0007
Penicillin-streptomycin	Merck	Cat# P0781
Puromycin	Invitrogen	Cat# A11138-03
Shandon Immu-Mount	Erpedia	Cat# 9990402
SiR-tubulin	Cytoskeleton, Inc.	Cat# CY-SC002
Sodium-selenite	Merck	Cat# S5261
Trifluoracetic Acid	Fluka	Cat# 40967–10X1ML-F
3,3′,5-Triiodo-L-thyronine sodium salt	Merck	Cat# T6397
Trypsin MS approved	Serva	Cat# 37286.04
Water for Chromatography LiChrosolv	Sigma-Aldrich	Cat# 1.15333.2500
Critical commercial assays		
DCTM Protein Assay Kit I	Bio-Rad	Cat# 5000111
Immobilon® -FL PVDF membrane	Sigma-Aldrich	Cat# 05317
Mini-PROTEAN® TGX™ Precast Gel 4-15% 10 wells	Bio-Rab Laboratories	Cat# 456-1083
Mini-PROTEAN® TGX™ Precast Gel 4-15% 15 wells	Bio-Rab Laboratories	Cat# 456-1086
PageRuler™ Plus Prestained Protein Ladder	Thermo Fischer Scientific	Cat# 26619
SuperSignal™ West Pico PLUS chemiluminescent Substrate	Thermo Fischer Scientific	Cat# 34580
Trans-Blot® Turbo™ Transfer Pack, Mini format 0.2 µm Nitrocellulose membranes	Bio-Rad Laboratories	Cat# 1704158
Deposited data		
GO annotation database	Ashburner et al.[83]; The Gene Ontology Consortium[84]	https://zenodo.org/records/14083199
Mass spectrometry data of large and small EVs isolated from serum-starved wild-type and Kif13b$^{-/-}$ mCCD cells	This study	MassIVE repository #MSV000098722 and ProteomeXchange #PXD066965
Experimental models: Cell lines		
mCCD wild type cells	Eric Féraille; Montesano et al.[42]	Wild type (parental)
mCCD Kif13b$^{-/-}$ cells	This study	Pool

(*Continued on next page*)

Continued

REAGENT or RESOURCE	SOURCE	IDENTIFIER
mCCD cells stably expressing mNG-KIF13B	This study	Pool
mCCD cells stably expressing mNG-KIF13B and mCherry-Rab8	This study	Pool
mCCD Kif13b$^{-/-}$ cells stably expressing mCherry-KIF13B	This study	Pool/rescue line
mCCD Kif13b$^{-/-}$ cells stably expressing mNG-KIF13B	This study	Pool/rescue line
mCCD Zdhhc5$^{-/-}$ cells	This study	Clone 22
mCCD cells stably expressing mNG-ZDHHC5	This study	Pool
HEK293T cells	ATCC	Cat#CRL-3216
IMCD3 wild type Flp-In cells	Maxence Nachury; Liew et al.[69]	Wild type (parental)
IMCD3 Arl6$^{-/-}$ Flp-In cells	Maxence Nachury; Liew et al.[69]	Arl6$^{-/-}$
IMCD3 Ift27$^{-/-}$ Flp-In cells	Maxence Nachury; Liew et al.[69]	Ift27$^{-/-}$
IMCD3 wild type Flp-In cells stably expressing mNG-ZDHHC5	This study	Pool
IMCD3 Ift27$^{-/-}$ Flp-In cells stably expressing mNG-ZDHHC5	This study	Pool
KM cells wild type	Phil Beales; Hernandez et al.[85]	Wild type (parental)
KM cells *Bbs4*$^{-/-}$	Phil Beales; Hernandez et al.[85]	*Bbs4*$^{-/-}$
KM cells *Bbs6*$^{-/-}$	Phil Beales; Hernandez-Hernandez et al.[85]	*Bbs6*$^{-/-}$
Oligonucleotides		
M. musculus Kif13b exon 17 sgRNA: 5'-caccgAGGAGAGCCG GTCCACACCG-3'5'-aaacCGGTGTGGACCGGCTCTCCTc-3'	Eurofins Genomics	sgRNA 1
M. musculus Kif13b exon 20 sgRNA: 5'-caccgTAACTTCACGT CATAAAACA-3'5'-aaacTGTTTTATGACGTGAAGTTAc-3'	Eurofins Genomics	sgRNA 2
M. musculus Kif13b exon 8 sgRNA: 5'-caccgATCATACAGAGT ATGTGTCA-3'5'-aaacTGACACATACTCTGTATGATc-3'	Eurofins Genomics	sgRNA 3
M. musculus Kif13b exon 25 sgRNA: 5'-caccgGACATTCTCGT GGATCTTAG-3'5'-aaacCTAAGATCCACGAGAATGTCc-3'	Eurofins Genomics	sgRNA 4
M. musculus Zdhhc5 exon 3 sgRNA: 5'-TTTATTGTCTACAGG TGTCC-3'	VectorBuilder	mZdhhc5[grna#86]
M. musculus Zdhhc5 exon 3 sgRNA : 5'-GCATTGTAAATGGG CACTGC-3'	VectorBuilder	mZdhhc5[grna#79]
Forward primer for ZDHHC5 with KpnI cutting site: 5'-CCGTC AGGTACCCCCGCAGAGTCTGGAAAG-3'	Eurofins Genomics	N/A
Reverse primer for ZDHHC5 with NotI cutting site: 5'-AGTCA CTGCGGCCGCTCACACAG-3'	Eurofins Genomics	N/A
Forward primer for KIF13B with KpnI cutting site: 5'-CAGGTA CCATGGGGGACTCCAAAGTGAAAGTGG-3'	Eurofins Genomics	N/A
Reverse primer for KIF13B with XbaI cutting site: 5'- CCTCTA GATCAGCTGGCCCAGGATTTCCGG -3'	Eurofins Genomics	N/A
Recombinant DNA		
H. sapiens KIF13B in pcDNA3	Joel Pomerantz; Lamason at al.[86]	
M. musculus ZDHHC5 in pNeo-Flag	Addgene; Tian et al.[87]	Cat# 85812
pSpCas9(BB)-2A-Puro (PX459) V2.0	Addgene; Ran et al.[88]	Cat# 62988
PX459 with *M. musculus Kif13b* guide 1 targeting exon 17	This study	LBP lab plasmid #943
PX459 with *M. musculus Kif13b* guide 2 targeting exon 20	This study	LBP lab plasmid #944
PX459 with *M. musculus Kif13b* guide 3 targeting exon 8	This study	LBP lab plasmid #945
PX459 with *M. musculus Kif13b* guide 4 targeting exon 25	This study	LBP lab plasmid #946
pRP[2CRISPR]-EGFP-hCas9-U6>mZdhhc5[grna#86, grna#79]	VectorBuilder	Cat#VB240527-1312thj
pENTR20-mCherry-C1 (Gateway)	Campeau et al.[89]	N/A
pENTR20-mNG-C1 (Gateway)	Campeau et al.[89]	N/A
pCDH-EF1A-GW-IRES-blast (Gateway)	Campeau et al.[89]	N/A
pCDH-EF1A-GW-IRES-neo (Gateway)	Campeau et al.[89]	N/A

(*Continued on next page*)

Continued

REAGENT or RESOURCE	SOURCE	IDENTIFIER
pMD2.G	Carlo Rivolta, Institute of Molecular and Clinical Ophthalmology, Basel, Switzerland	N/A
pCMVΔ-R8.2	Carlo Rivolta, Institute of Molecular and Clinical Ophthalmology, Basel, Switzerland	N/A
mCherry-KIF13B in pCDH-EF1A-GW-IRES-blast	This study	LBP lab plasmid #1060
mNG-KIF13B in pCDH-EF1A-GW-IRES-blast	This study	LBP lab plasmid #1056
GFP-CCDC92	Lukas Cajanek; Bernatik et al.[53]	N/A
mNG-ZDHHC5 in pCDH-EF1A-GW-IRES-blast	This study	LBP lab plasmid #1205
Software and algorithms		
Adobe Illustrator	Adobe	Version 29.1
Adobe Photoshop	Adobe	Version 25.12.0
cellSense	Evident	Version 1.18
CiliaQ (FIJI plugin)	Hansen et al.[66]	Version 0.1.7; https://github.com/hansenjn/CiliaQ
CiliaQ Editor (FIJI plugin)	Hansen et al.[66]	Version 0.1.7; https://github.com/hansenjn/CiliaQ_Editor
CiliaQ_Preparator (FIJI plugin)	Hansen et al.[66]	Version 0.1.2; https://github.com/hansenjn/CiliaQ_Preparator
FIJI (Image J)	Schindelin et al.[90]	https://imagej.net/ij/
GraphPad Prism	GraphPad Software Inc.	Version 7.0
GraphPad Prism	GraphPad Software Inc.	Version 10.0.5 (673)
DIA-NN	Demichev et al.[91]	Version 1.9.2; https://github.com/vdemichev/DiaNN
MaxQuant	Cox et al.[92]	Version 1.6.1.0
PANTHER Overrepresentation Test	Thomas et al.[93]	Version released version released 20240807; https://geneontology.org/
Perseus	Tyanova et al.[94]	Version 1.6.15.0
ZetaView	Particle Metrix	Version 8.05.16 SP3
Other		
Mini-PROTEAN® Tetra System	Bio-Rad Laboratories	Cat# 1658005EDU
50cm µPAC nanoLC column	Thermo Fisher Scientific	Cat# COL-NANO050G1B
Trans-BLOT® Turbo Transfer System	Bio-Rad Laboratories	Cat# 1704150
µPAC Trapping column nano 1/16″	Thermo Fisher Scientific	Cat# COL-TRPNANO16G1B2

EXPERIMENTAL MODEL AND STUDY PARTICIPANT DETAILS

Cell lines and culture media

Mouse cortical collecting duct cells (mCCD)

Immortalized mCCD were generously provided by Dr. Eric Féraille from University of Lausanne, Switzerland, and have been described previously.[42] mCCD cells were grown at 37 °C with 5% humidified CO_2 in DMEM/F12 with GlutaMaX (Thermo Fisher Scientific, Cat#10565018) supplemented with 2% fetal bovine serum (FBS, heat inactivated, Merck), 5 µg/ml insulin (Merck, Cat#I6634), 5 µg/ml holo-transferrin (Merck, Cat#T0665), 5 ng/ml EGF (Merck, Cat #SRP3196), 50 nM dexamethasone (Merck, Cat #D4902), 60 nM sodium selenite (Merck, Cat#S5261), 1 nM 3,3′,5-Triiodo-L-thyronine sodium salt (Merck, Cat#T6397), and 1% penicillin-streptomycin (Merck, Cat#P0781). To promote ciliation, mCCD cells were grown to ca. 80% confluency and then cultured at 37 °C with 5% humidified CO_2 for 24, 48 or 72 h in DMEM/F12 – GlutaMaX supplemented with 60 nM sodium selenite and 5 µg/ml holo-transferrin.

Mouse inner medullary collecting duct cells (IMCD3)

WT and Arl6$^{-/-}$ and Ift27$^{-/-}$ IMCD3 Flp-In cell lines were kindly supplied by Dr. Maxence Nachury from the University of California, San Francisco (UCSF), USA.[69] The cells were cultured at 37 °C with 5% humidified CO_2 in DMEM/F-12, GlutaMAX Supplement (Gibco, Cat#31331-093) medium supplemented with 10% fetal bovine serum (FBS; Gibco, Cat #10438-026) and 1% Penicillin-Streptomycin

(Sigma-Aldrich, Cat#P0781). To promote ciliation, IMCD3 cells were grown to ca. 80% confluency and then cultured at 37 °C with 5% humidified CO_2 for 24 or 72 h in DMEM/F12 – GlutaMaX without supplements.

Human embryonic kidney 293T cells (HEK293T)

HEK293T cells were from ATCC (cat# CRL-3216) and were cultured at 37 °C with 5% humidified CO_2 in high-glucose DMEM (Gibco, Cat#41966-052) supplemented with 10% FBS (Gibco, Cat #10438-026) and 1% Penicillin-Streptomycin (Sigma-Aldrich, Cat#P0781).

Mouse kidney medullary cells (KM)

WT and *Bbs4*$^{-/-}$ and *Bbs6*$^{-/-}$ cells have been described in[19] and were cultivated at 37 °C with 5% humidified CO_2 in DMEM/F-12 (Thermo Fisher Scientific, Cat#11320033).

METHOD DETAILS

Transfections and drug treatment

For transfection of kidney cell cultures, we used Lipofectamine 3000 (Thermo Fischer Scientific; Cat#L3000015) according to the guidelines provided by the manufacturer. For selection of transfected cells, blasticidin (Gibco; Cat#r210-01) was used at a concentration of 5-15 μg/ml and puromycin (Invitrogen, Cat#A11138-03) was used at 2 μg/ml. SiR-tubulin dye (Cytoskeleton, Inc., Cat#CY-SC002) was added to cell culture medium to a final concentration of 1 μM. GW4869 treatment of cells for NTA analysis was performed by treatment with 10 μM GW4869 (Sigma-Aldrich, Cat#D1692) dissolved in DMSO during serum starvation (24 h) prior EV preparation. For drug treatment of mCCD cells for IFM, we used ML141 (Tocris; Cat#4266), dynasore (Sigma-Aldrich; Cat#D7693), or GW4869 (Sigma-Aldrich; Cat#D1692), on cells that were serum starved for 24 h. GW4869 treatment was performed with 10 μM of drug, overnight during serum starvation. All other cells were treated for 3 additional hours after serum starvation, with 50 μM ML141 or 40 μM dynasore, before fixation for IFM.

Gene knockout and rescue

To knock out *Kif13b* in mCCD cells, we utilized four sgRNA sequences from the mouse CRISPR "Brie" Knockout Library.[95] The specific sequences are provided in the Key Resources Table. The sgRNA spacers were cloned into pSpCas9(BB)-2A-Puro (PX459) V2.0 plasmid (Addgene, Cat#62988;[88]) by phosphorylating and annealing the two complementary sgRNA oligos, followed by ligation into the BbsI-digested vector. After transformation into *Escherichia coli* DH10B cells (lab stock), plasmids from selected clones were purified and sequenced by Eurofins to verify the spacer sequence. The parental (WT) mCCD cells were transfected with the Cas9-gRNA plasmids (pool of all four gRNAs) using Lipofectamine 3000 Transfection Reagent (Invitrogen, Cat#L3000015) as per the manufacturer's instructions. One day after transfection, cells were treated with 2 μg/ml puromycin (Invitrogen, Cat#A11138-03) for 72 h and then tested for KIF13B protein depletion by western blot analysis. Selected clones were sorted with a FACS Aria III instrument at the FACS Facility at Biotech Research & Innovation Centre (University of Copenhagen, Copenhagen, DK) and pooled prior to use in experiments.

To knock out *Zdhhc5* Mammalian CRISPR Vector (Dual gRNA) was customized from VectorBuilder using the function "Design My Vector" and purchased. The plasmid codes for a Cas9-GFP fusion protein and two sgRNA against *Zdhhc5* exon 3, from the VectorBuilder database. The specific sequences are provided in Key Resources Table. Briefly, mCCD cells were transfected with the plasmid using Lipofectamine 3000 Transfection Reagent (Invitrogen, Cat#L3000015) as per the manufacturer's instructions. A day after transfection the GFP positive cells were FACS sorted into single cells in a 96 well plate with a FACS Aria III instrument at the FACS Facility at Biotech Research & Innovation Centre (University of Copenhagen, Copenhagen, DK). When cells reached confluency they were sub-cultured in two 96 well plates. One plate was used to screen the clones for ZDHHC5 depletion by western blot analysis, the other plate was used to keep the clones in culture. Three knock-out clones were expanded and sent for Sanger sequencing at Eurofins Genomics. The clone that we used for this study (clone 22) has a deletion of 31 bp in exon 3 leading to a frameshift (Figure S5E).

To create transgenic cell lines for live-cell imaging and/or rescue experiments, we generated lentiviral expression constructs coding for mNG-KIF13B, mCherry-KIF13B or mNG-ZDHHC5, expressed under EF1a and IRES promoters to ensure low and stable expression.[96] In summary, the full-length human *KIF13B* or mouse *Zdhhc5* coding sequence was cloned into pENTR-mCherry-C1 or pENTR-mNG-C1 using standard cloning techniques. Primers utilized for this process are detailed in Key Resources Table. The resulting Gateway entry plasmids were further recombined with the pCDH-EF1a-Gateway-IRES-BLAST destination plasmid using the Gateway LR recombination kit (Invitrogen, Cat#11791020). All cloning vectors were kindly supplied by Dr. Kay Oliver Schink, Oslo University Hospital, Norway, and were described in Campeau et al.[89]. To generate lentiviruses, lentiviral expression plasmids were co-transfected with packaging plasmids pMD2.G and pCMVΔ-R8.2 (kind gift of Dr. Carlo Rivolta, Institute of Molecular and Clinical Ophthalmology Basel, Switzerland) into HEK293T cells using Lipofectamine 3000 (Invitrogen, Cat#L3000015). The clarified culture medium containing the lentivirus particles was subsequently used to transduce IMCD3 WT, IMCD3 *Ift27*$^{-/-}$, mCCD WT, and mCCD Kif13b$^{-/-}$ cells. Expressing cells were selected using blasticidin (Gibco; Cat#r210-01) at a concentration of 5-15 μg/ml, and successful expression was confirmed through western blotting and IFM.

SDS-PAGE and western blotting

SDS-PAGE and western blotting of cell lysates were performed as follows using antibodies listed in the Key Resources Table. Cells were lysed with 95 °C SDS-lysis buffer (1% SDS, 10 mM Tris-HCl, pH 7.4), transferred to Eppendorf tubes and incubated shortly at 95 °C. DNA was sheared by sonicating two times for 30 seconds and debris removed after centrifugation at 20,000 x *g* for 15 min at room temperature. Protein concentrations were determined with the *DC*™ Protein Assay Kit I from Bio-Rad (Cat# 5000111) by following the manufacturer's protocol. Lysates were prepared for SDS-PAGE analysis by adding NuPAGE™ LDS Sample Buffer (4X) from Thermo Fischer Scientific (Cat#NP0007) and 50 mM DTT, followed by heating at 95 °C for 5 minutes. SDS-PAGE was performed with the Mini-PROTEAN® Tetra System and Mini-PROTEAN® TGX™ Precast Gel 4-15% 10 wells and 15 wells from Bio-Rab Laboratories, Inc. (Cat#456-1083 and Cat#456-1086). PageRuler™ Plus Prestained Protein Ladder (Thermo Fischer Scientific, Cat#26619) was used as molecular mass marker. The Trans-BLOT® Turbo Transfer System from Bio-Rad Laboratories, Inc. was used for transferred of proteins from gels from onto Trans-Blot® Turbo™ Transfer Pack, Mini format 0.2 μm Nitrocellulose membranes (Bio-Rad Laboratories, Inc.; Cat#1704158). Membranes were blocked in 5% milk or 5% bovine serum albumin (BSA) in Tris-buffered saline with Tween-20 (TBS-T; 10 mM Tris-HCl, pH 7.5, 150 mM NaCl, 0.1% Tween-20) for 2 hours at room temperature and then incubated overnight at 4 °C with primary antibodies (see Key Resources Table) diluted in 5% milk or 5% BSA (according to the antibody compatibility found on the datasheet) in TBS-T. Membranes were washed three times 10 min at room temperature in TBS-T prior to incubation with secondary antibodies (see Key Resources Table) diluted in 5% milk or 5% BSA in TBS-T for 1 hour at room temperature. Finally, after three times 10 min washes at room temperature in TBS-T, blots were developed with SuperSignal™ West Pico PLUS chemiluminescent Substrate (Thermo Fischer Scientific, Cat#34580) using a FUSION FX SPECTRA machine from Vilber. SDS-PAGE and western blotting of large and small EVs purified by lectin-mediated precipitation were done in a similar manner. For western blot analysis of small EVs purified by ultracentrifugation, small EV pellets were resuspended in loading buffer (0.125 M Tris-HCl, 20% (v/v) glycerol, 0.004% (w/v) bromphenol blue) run on a 10% SDS-PAGE and transferred to a PVDF membrane (Immobilon® -FL PVDF membrane, Sigma-Aldrich, Cat#05317). The membrane was blocked with blocking buffer (0.5% Casein; 0.1% Tween; 0.04% NaN_3; 150 mM NaCl) and incubated with primary (overnight, 4°C) and secondary antibodies (1 h), listed in the Key Resources Table. Fluorescence detection was carried out using Odyssey Fc Imaging System (LICOR Bioscience).

Microscopy

Immunofluorescence microscopy

Kidney epithelial cells were grown to ca. 80% confluency and then serum- and hormone-deprived for 24 or 72 h. Unless otherwise indicated, cells were first fixed with 4% PFA for 15 min at room temperature or 20 min at 4 °C followed by permeabilization with 1% BSA and 0.2 % Triton X-100 in PBS for 12 min. Permeabilized cells were blocked in 2% BSA blocking buffer for 1 h at room temperature. Cells were then incubated 1-2 h at room temperature or overnight at 4 °C with primary antibodies diluted in blocking buffer. KM cells were permeabilized in PBS with 0.3% Triton-X and for blocking and staining, fishblock solution with 0.3% Triton-X 100 was used. After several washes in PBS, cells were next incubated with secondary antibodies diluted in 2% BSA in PBS for 1 h at room temperature. Finally, nuclei were stained with DAPI (Sigma-Aldrich, Cat#D9542). Coverslips were mounted on slides with Shandon Immu-Mount (Thermo Scientific, Cat #9990402) supplemented with 0.5% N-propyl gallate.

For PC2 staining, we used an IFM protocol method described in[44] where we pre-fixed cells with 0.4% PFA for 5 min at 37 °C, permeabilized with PHEM buffer (50 mM PIPES; 50 mM HEPES; 10 mM $MgCl_2$; pH 6.9) containing 0.5% Triton X-100 for 5 min at 37 °C, followed by a 4% PFA fixation for 15 min at room temperature. For HGS staining, we followed an IFM protocol method described in[97] where we briefly washed the cells with cytoskeletal buffer, then immediately fixed them with ice-cold MeOH inside a −20 °C freezer for 10 min. Imaging of IFM samples was done using an Olympus IX83 inverted microscope, equipped with a Yokogawa CSU-W1 confocal scanner unit, ORCA-Flash4.0 V3 Digital CMOS camera (type number: C13440-20CU), and Olympus UPlanSApo 100x oil microscope objective. For figure preparation, we used cellSens version 1.18 software (Evident) for constrained iterative deconvolution and assembled images for figures with FIJI,[90] Adobe Photoshop version 25.12.0 (Adobe) and Adobe Illustrator version 29.1 (Adobe).

Time lapse live cell imaging

To observe KIF13B, ZDHHC5 and CCDC92 dynamics in the primary cilia of kidney epithelial cells, we used mCCD cells stably expressing mNG-KIF13B, IMCD3 and mCCD cells stably expressing mNG-ZDHHC5, and mCCD cells transiently transfected for 24 h with Lipofectamine-3000 and 2 μg of GFP-CCDC92 plasmid. The primary cilia were visualized using SiR-tubulin staining. Cells were cultured on a 35 mm glass-bottom dishes and serum-starved for 24-72 h. For staining with SiR-tubulin dye (Cytoskeleton, Inc., Cat#CY-SC002), culture medium was supplemented with 1 μM of SiR-tubulin and cultures incubated in a cell incubator at 37 °C in a humidified atmosphere containing 5% CO_2 for at least 30 min prior to cell imaging. Imaging was performed in a humidity chamber on an Olympus inverted microscope (IX83) equipped with Yokogawa spinning disc with 100× oil objective. The 488 nm and 640 nm laser lines were used for imaging mNG/GFP and SiR-Tubulin-Cy5, respectively. mCCD cells stably expressing mNG-KIF13B, which were serum starved for 24 h, were imaged using the Hamamatsu ORCA-Flash 4.0 digital camera (C13440) using the confocal settings at 5-10 sec time intervals. The rest of the cell lines and serum-starved conditions were imaged with the Teledyne Prime 95B back-illuminated sCMOS camera (01-PRIME-95B-R-M-16-C) using confocal settings at 3 sec time intervals for mNG-ZDHHC5 and 0.5 sec frame rate for GFP-CCDC92.

Scanning electron microscopy (SEM)

To prepare the samples for SEM imaging, mCCD cells grown on glass coverslips and serum starved for 24 h or 72 h were fixed in 2% glutaraldehyde in 100 mM sodium cacodylate at room temperature for at least 2 h up to several days. Subsequently, cells were washed three times in 100 mM sodium cacodylate and then treated with 1% OsO_4 in 100 mM sodium cacodylate for 1-2 h at room temperature. The cells were then washed with deionized water and dehydrated with a graded series of ethanol solutions (30%, 50%, 70%, 80%, 95%, and 100%) at room temperature, with each step lasting 5-10 min. The samples were allowed to dry using a critical point drier. Dried samples were mounted onto stubs and sputter coated with 6 nm gold. The coated samples were then placed into a SEM chamber and images captured with a FEI Quanta 3D FEG dual beam SEM microscope (University of Copenhagen's Core Facility for Integrated Microscopy).

Transmission electron microscopy (TEM)

Small and large EV pellets isolated by ultracentrifugation from spent media following 48 h or 24 h serum-starvation were resuspended in particle-free PBS. They were subsequently applied to 400 mesh carbon-coated copper grids (Electron Microscopy Science) and allowed to settle for 1 min. Embedded EVs were fixed with 1% glutaraldehyde for 5 min and washed four times with deionized water (ddH_2O). Negative staining was performed by applying 2% uranyl acetate for 1 min and the grids were allowed to dry. Imaging was done with a FEI Tecnai G2 12 BioTwin transmission electron microscope (Fei, Company, Hillsboro, USA).

Purification of extracellular vesicles

Large EVs for MS analysis were purified by differential centrifugation of spent medium from 24 or 72 h serum-starved mCCD cells. To remove cell debris, the medium was first centrifuged at 2,000 x *g* for 20 min. This higher-speed initial centrifugation was chosen to improve the purity of the final pellet by reducing contamination from smaller debris. The supernatant, containing large EVs, was carefully transferred without disturbing the pellet. Large EVs and particles were then collected by centrifugation at 10,000 x *g* for 50 min at 4 °C and resuspended in 6 M Urea-Tris buffer (0.4 M Tris pH 7.8; 6 M urea) for further MS analysis. To purify small EVs for NTA, TEM and MS analysis we used a previously published ultracentrifugation approach.[19] Briefly, spent medium was collected from 24, 48 or 72 h serum-starved mCCD cultures and first centrifuged at 1,000 x *g* for 10 min to remove cell debris. The supernatant was collected and subjected to further centrifugation at 10,000 x *g* for 30 min at 4 °C to sediment large EVs and particles. The supernatant was then subjected to ultracentrifugation at 100,000 x *g* for 2 h at 4 °C to sediment small EVs (Optima L-80K ultracentrifuge, Beckman Coulter, swing bucket SW28 rotor or Optima MAX-E ultracentrifuge, Beckmann Coulter, TLA-55 fixed-angle rotor). The final pellet was resuspended in particle-free PBS, Laemmli buffer or 6 M Urea-Tris buffer and used for downstream analyses.

To purify large and small EV for western blot analysis (Figure S3B), we used a combined centrifugation and lectin-mediated precipitation approach.[50] Spent medium from 72 h serum-deprived mCCD cultures was first centrifuged at 3,000 x *g* for 30 min to remove cell debris. The supernatant was then centrifuged for 40 min at 10,000 x *g* to sediment large EVs, which were collected, resuspended in PBS supplemented with protease inhibitor and centrifuged again for 60 min at 20,000 x *g* prior to SDS-PAGE and western blot analysis. Meanwhile, 1 μg/ml Concanavalin A from *Canavalia ensiformis* (Sigma-Aldrich, cat. # C2010) was added to the supernatant and the mixture put on slow stir for 16 h at 4 °C. Subsequently, small EVs were collected by centrifugation for 60 min at 14,000 x *g*. The pellet was resuspended in PBS supplemented with protease inhibitor and centrifuged again for 60 min at 20,000 x *g* prior to SDS-PAGE and western blot analysis.

Nanoparticle tracking analysis (NTA)

Small and large EVs were isolated by ultracentrifugation from spent media of 24, 48 and 72 h serum-deprived mCCD cells. Inhibition of EV release was performed by treatment with 10 μM GW4869 (Sigma-Aldrich, cat. #D1692) dissolved in DMSO during serum starvation (24 h) prior EV preparation. Particles were resuspended in particle-free PBS and measured using ZetaView Nanoparticle Analyzer PMX-230 (TWIN) (Particle Metrix). Particle movement was recorded in scatter mode 1-2 Cycles at 11 Positions, at a steady temperature of 25°C and analysed using the Software ZetaView (version 8.05.16 SP3). Settings were adjusted and adapted for particle size as recommend by the manufacturer. For both the small and large EV samples, the instrument sensitivity and shutter speed were set to 80 and 100 ms, respectively, and video capture was performed at 30 frames per second with the high-resolution mode enabled.

The minimum brightness threshold was fixed at 30 arbitrary units for the small EV samples, while analysis of the large EV samples used the software's automatic brightness setting. Particle-size filters differed: the small EV analysis accepted particles with an area between 10 pixel and 1000 pixel, whereas the large EV analysis was restricted to particles ranging from 40 pixel to 2000 pixel. Finally, the tracking algorithm was configured to follow each particle for up to 15 frames in the small EV protocol and for up to 30 frames in the large EV protocol.

Liquid chromatography (LC)-MS/MS analysis

Chemicals used for MS analysis include: acetonitril LC-MS-grade, Chromasolv (Sigma-Aldrich; Cat#349672.5L), 1,4-Dithiothreitol (Merck, Cat# 1.11474.0025), formic acid, 99.0%, Optima, LC-MS grade (Fischer Scientific, Cat#A11750), 2-Iodacetamide (Merck, Cat# 8.04744.0025), Trifluoracetic Acid (Fluka; Cat# 40967-10X1ML-F), Trypsin MS approved (Serva; Cat#37286.04) and Water for Chromatography LiChrosolv (Sigma-Aldrich; Cat# 1.15333.2500).

Small EV pellets from spent medium of serum-deprived mCCD cells (n=4/cell line, 24 h and 72 h) were isolated using ultracentrifugation. Pellets were diluted in 6 M Urea-Tris buffer and subjected to liquid chromatography-MS analysis as described previously.[19]

For analysis of large EVs isolated by centrifugation, the protein samples were subjected to proteolytic cleavage as described earlier[19] before the resulting peptides were analysed by LC-MS. Peptide separation was performed using a nanoElute 2 LC system (Bruker) coupled to a timsTOF Ultra 2 mass spectrometer (Bruker). A trap-column chromatography setup was employed, consisting of a Thermo Trap Cartridge (5 mm) for sample trapping and a PepSep Twenty-five Series analytical column (75 μm ID, 1.5 μm particle size). The column temperature was maintained at 50 °C throughout the analysis.

Samples were loaded using an ultra-low volume (μl) pickup injection method, with a total sample loading volume of four pick-up cycles plus two microliters. Chromatographic separation was performed at a constant flow rate of 0.30 μl/min, using a gradient elution with mobile phase A consisting of 0.1% formic acid in water and mobile phase B of 0.1% FA in 99.9% acetonitrile. The gradient started at 5% B, increasing to 25% B at 24 min, then to 35% B at 30 min, and reaching 95% B at 34 min, where it was held until 38 min before re-equilibrating to 5% B at 40 min.

Data acquisition was performed in DIA-PASEF mode (Data-Independent Acquisition Parallel Accumulation–Serial Fragmentation).[98] Ionization was performed using a CaptiveSpray nanoelectrospray source, with a capillary voltage of 1600 V. The dry gas flow rate was set to 3.0 l/min, and the drying temperature was maintained at 200 °C. The instrument was operated in positive ion mode, with Trapped Ion Mobility Spectrometry (TIMS) enabled to enhance precursor separation and fragmentation efficiency. Spectra were acquired across a mass range of 100 to 1700 m/z, with an ion mobility range (IM) from 0.60 to 1.40 Vs/cm^2. The accumulation time per scan was 2.0 milliseconds, with a ramp time of 100.0 milliseconds. Each acquisition cycle included 12 DIA-PASEF scans, resulting in a total cycle time of approximately 1.38 seconds. DIA windows were dynamically adjusted based on precursor density, covering an m/z range of 300 to 1200. Fragmentation was conducted using collision-induced dissociation (CID), with collision energy dynamically adjusted as a function of ion mobility. High-sensitivity detection mode was enabled to maximize signal acquisition efficiency.

QUANTIFICATION AND STATISTICAL ANALYSIS

MS data analysis

Data-independent acquisition (DIA) data were processed using DIA-NN (Data-Independent Acquisition by Neural Networks)[91] version 1.9.2. The analysis was performed using a reference spectral library generated in silico from the Swissprot Mouse FASTA database (version 12/2024) and common contaminants database included in DIA-NN and refined empirically from the acquired DIA data. Search settings included N-terminal methionine excision, cleavage specificity at lysine (K) and arginine (R) with one missed cleavage allowed, and cysteine carbamidomethylation as a fixed modification. Variable modifications were restricted to one per peptide. The precursor and fragment mass accuracies were set to 15 ppm, Match Between Runs (MBR) and peptidoform-level scoring were enabled. Protein inference was performed using heuristic protein grouping, reducing redundancy while preserving quantitative accuracy. False discovery rate (FDR) filtering was applied at 1% at the precursor and protein levels.

Spectral library generation and retention time alignment were performed during a first-pass search, followed by reanalysis using the empirically refined library. Quantification was carried out at the precursor, protein, and gene levels. The "PG.MaxLFQ" expression matrix output reports normalized quantity employing the MaxLFQ principle[99] was used for quantitative analysis on the protein level for downstream statistical analysis. Ratio, t-test and significance A were calculated using the Perseus framework.[94] Only proteins identified and quantified in more than 50% of the samples were considered. Missing values were replaced before statistical testing. For both statistical tests, correction for multiple testing was performed (t-test: permutation-based FDR; Significance A: Benjamini-Hochberg FDR). Proteins, detected to be significant for both tests after FDR determination with an FDR of 0.05 were considered as Tier 1 hits. Proteins with a p-value < 0.05 for both tests without FDR determination were considered as Tier 2 hits.

For Data S1 and Data S2, up- and down regulated protein are colour coded differently. Tier 1 hits upregulated in dark green, down regulated in light green. Tier 2 hits up regulated in orange, down regulated in yellow.

GO term enrichment analysis

Gene ontology (GO) term enrichment analysis was performed using the PANTHER Overrepresentation Test.[93] The analysis was conducted on a gene list derived from *Mus musculus* using the complete *Mus musculus* gene database as the reference list. The GO annotation database used was DOI: https://doi.org/10.5281/zenodo.14083199, released on 2024-11-03.[83,84] Statistical significance was assessed using Fisher's exact test, and multiple testing correction was applied using the FDR method. We searched for GO term enrichment for the categories molecular function and cellular component.

IFM and SEM data analysis

Unless stated otherwise, quantitative analysis of IFM images was done using FIJI software[90] to measure ciliary length, frequency, and relative mean fluorescence intensity (MFI) of relevant antibody-labeled antigens within or at the base of cilia in WT, mutant and rescue cell lines. Non blinding was done. IFM images of HGS and ZDHHC5 staining in IMCD3 cells were analyzed by a semi-automated method using the CiliaQ plugin[66] on ImageJ. Rapidly, for each stack, borders were cropped, and the image center was treated with the CiliaQ Preparator v0.1.2 plugin, to detect and generate masks of cilia. The following parameters were used: Segmentation style: Set intensities above thresholds to maximum possible intensity value (creates a binary image). Channel duplicated to include a copy of the channel that is not segmented. Subtract Background: 20. Segmentation method: Canny 3D Thresholder, (plugin by Sebastian Rassmann, see https://github.com/sRassmann/canny3d-thresholder for a description). Gauss sigma:1.0. Canny alpha: 5.0.

Low threshold method (hysteresis thresholding): IsoData. High threshold method (hysteresis thresholding): Otsu. The results images were treated by the CiliaQ Editor v0.0.3 plugin and unwanted detected object were discarded. Finally, we used the CiliaQ v0.1.7 plugin to extract protein of interest fluorescence intensities inside cilia masks.[66] For each cilium, integrated fluorescence intensities were normalized by the average fluorescence intensities inside the cilium. For each experiment, intensities were further normalized to relevant control/WT condition. Each dot corresponds to one cilium and plotted data on graph originate from three independent experiment. For ciliary length and PC2 staining in WT and Zdhhc5$^{-/-}$ mCCD cells, as well as for PC2 quantification upon endocytosis and ectocytosis inhibitor treatment, the same approach was used but Triangle and Otsu methods were used for the low and high threshold parameters respectively in CiliaQ preparator plugin. In inhibitors experiments, for each cilium, average background intensity was subtracted to the average intensity of the 10% of voxels with brightest intensity inside the cilium to obtain a corrected average intensity of PC2 for each cilium.

Quantitative analysis of SEM data was done using FIJI software[90] to measure ciliary length, and manually to quantify ciliary membrane bulges. Unless stated otherwise in the figure legends, at least three independent biological replicates were analyzed. Statistical analyses were performed using GraphPad Prism version 10.0.5 (673) (GraphPad Software, Inc.) and the specific parameters defined in the figure legends.

Western blot data analysis

For quantitative analysis of western blot data we used Fiji software[90] to measure the average pixel intensity of the bands. Subsequently, we normalized the acquired numbers to the loading control and performed the statistical analysis in GraphPad Prism version 10.0.5 (673) (GraphPad Software, Inc.) using the parameters specified in the figure legends. Unless otherwise stated, the results were confirmed in at least three independent biological replicates.

NTA data analysis

Statistical analysis on NTA data was done in Graphpad Prism 7.0 software (Graphpad Software Inc.). Outliers were excluded using the ROUT method (Q = 1%). Gaussian distribution was tested using Shapiro-Wilk and Kolmogorov-Smirnov test ($P < 0.05$). For Gaussian distributed data, *t* test and for non-Gaussian distributed data, Mann-Whitney *U* test performed.

Significance levels

$P > 0.05$ not significant (ns), $P \leq 0.05$ *, $P \leq 0.01$ **, $P \leq 0.001$ ***, $P \leq 0.0001$ ****.